J. Fluid Mech. (2011), *vol.* 681, *pp.* 261–292. © Cambridge University Press 2011
doi:10.1017/jfm.2011.196

A study of Mach wave radiation using active control

M. KEARNEY-FISCHER, J.-H. KIM AND M. SAMIMY†

Gas Dynamics and Turbulence Laboratory, Department of Mechanical and Aerospace Engineering, The Ohio State University, 2300 West Case Road, Columbus, OH 43235-7531, USA

(Received 15 October 2010; revised 17 April 2011; accepted 27 April 2011; first published online 13 June 2011)

Mach wave radiation is one of the better understood sources of jet noise. However, the exact conditions of its onset are difficult to determine and the literature to date typically explores Mach wave radiation well above its onset conditions. In order to determine the conditions for the onset of Mach wave radiation and to explore its behaviour during onset and beyond, three ideally expanded jets with Mach numbers $M_j = 0.9$, 1.3 and 1.65 and stagnation temperature ratios ranging over $T_o/T_\infty = 1.0$–2.5 (acoustic Mach number 0.83–2.10) were used. Data are collected using a far-field microphone array, schlieren imaging and streamwise two-component particle image velocimetry. Using arc filament plasma actuators to force the jet provides an unprecedented tool for detailed examination of Mach wave radiation. The response of the jet to various forcing parameters (combinations of one azimuthal mode $m = 0$, 1 and 3 and one Strouhal number $St_{DF} = 0.09$–3.0) is explored. Phase-averaged schlieren images clearly show the onset and evolution of Mach wave radiation in response to both changes in the jet operating conditions and forcing parameters. It is observed that Mach wave radiation is initiated as a coalescing of the near-field hydrodynamic pressure fluctuations in the immediate vicinity of the large-scale structures. As the jet exit velocity increases, the hydrodynamic pressure fluctuations coalesce, first into a curved wavefront, then flatten into the conical wavefronts commonly associated with Mach wave radiation. The results show that the largest and most coherent structures (e.g. forcing with $m = 0$ and $St_{DF} \sim 0.3$) produce the strongest Mach wave radiation. Conversely, Mach wave radiation is weakest when the structures are the least coherent (e.g. forcing with $m = 3$ and $St_{DF} > 1.5$).

Key words: aeroacoustics, instability control, jet noise

1. Introduction

The noise from a turbulent jet consists of several major components. It is well established that there exist flow structures ranging in size from dissipation-scale to the order of the nominal exit dimension of the jet nozzle. It is generally accepted that jet noise is produced by the interaction, as well as disintegration, of these structures. Beyond this point, the description of noise production processes gets quite complicated. In subsonic jets, the interaction and disintegration of flow structures produce what is known as mixing noise. A supersonic jet could also include screech

† Email address for correspondence: samimy.1@osu.edu

https://doi.org/10.1017/jfm.2011.196 Published online by Cambridge University Press

tones and broadband-shock-associated noise. Depending on the velocity of the jet and the acoustic properties of the fluid into which the jet is exhausting, there is yet another noise component known as Mach wave radiation. In some operating regimes, Mach wave radiation is the dominant noise component (Tam 1995). Some of these noise production mechanisms are fairly well understood while others are not; and the interdependence of the various mechanisms is not easily identified. The purpose of this paper is to use active control on both subsonic and supersonic jets over a range of temperatures and Mach numbers to explore the nature of Mach wave radiation. As will be seen, forcing the jet results in Mach wave radiation that is isolated to frequencies at or above the forcing frequency (at least for frequencies near the jet column natural frequency $St_D = 0.3$). This allows the indicators of Mach wave radiation to be concentrated into a smaller portion of the spectrum resulting in easier identification of their existence. Forcing also provides a well-defined phase relationship allowing for phase-locked data acquisition for a better understanding of the jet dynamics and the radiated noise.

2. Background

2.1. *Mach wave radiation*

Mach wave radiation is one of the better understood aspects of jet noise. As explained in detail in the review papers of Tam (1991, 1995), Mach wave radiation is produced by a flow perturbation which travels supersonically relative to the surrounding fluid. In jets, this traditionally translates into flow structures (i.e. large-scale structures) in the mixing layer moving supersonically with respect to the ambient air (in a single-stream configuration). The mathematical formalism with which this problem is typically tackled (e.g. Tam 1971; Tam & Burton 1984; Tam, Ghen & Seiner 1992; Seiner, Bhat & Ponton 1994; Wu 2005) examines the growth, decay and propagation velocity (phase velocity) of a perturbation of a particular frequency (i.e. instability wave). This approach is usually referred to as the wavy wall analogy. These forms of stability analysis have shown that there exist three different families of instability waves, each with their own characteristics (Tam & Hu 1989). This theoretical framework has been validated by a number of experiments (e.g. Tam & Burton 1984; Tam & Hu 1989; Tam *et al.* 1992). The validation has been somewhat limited in choices of perturbation frequency, azimuthal mode and operating conditions, but the results are generally positive.

Previous works (e.g. Morrison & McLaughlin 1979; Papamoschou & Debiasi 2001) have experimentally constructed estimates for the onset of Mach wave radiation. Papamoschou & Debiasi (2001) state that jets with acoustic Mach numbers (defined as the jet exit velocity divided by the ambient speed of sound), M_a, greater than about 1.3 will produce Mach wave radiation. A different Mach number, originally defined by Oertel (1982) as $w'/a_\infty \equiv M_{co}$(see (4.3)), was used by Krothapalli, Arakeri & Greska (2003) to estimate that Mach wave radiation should be present in jets with $M_{co} \geqslant 1.25$.

Authors such as Krothapalli *et al.* (2003), Greska *et al.* (2008), Papamoschou (1997) and Papamoschou & Debiasi (1999) have noted changes in the characteristic shape of the far-field spectra in the peak radiation direction. It was observed that, compared to a jet which is free of Mach wave radiation, the range of peak radiation frequencies is broader and flatter and the slope of the high-frequency roll-off is less steep. Greska *et al.* (2008) discuss these changes in terms of two characteristic spectral shapes for the peak radiation direction and analyse sound intensity normalization across a wide range of velocities using a convective Mach number definition they refer to as

https://doi.org/10.1017/jfm.2011.196 Published online by Cambridge University Press

the Oertel convective Mach number. Papamoschou & Debiasi (1999) used a tuned secondary stream to dramatically reduce the amount of Mach wave radiation by creating two acoustically subsonic shear layers in place of one which was acoustically supersonic.

The mathematical framework that gives rise to Mach wave radiation has also been used in recent years to offer an explanation for directional radiation in an acoustically subsonic jet (e.g. Tam 1995; Avital, Sandham & Luo 1998; Obrist 2009; Tam 2009). The basic construction of this discussion has been that a single perturbation frequency should be broadened by the spatiotemporal variation of amplification in the jet. Avital *et al.* (1998) described two domains of Mach wave radiation: the subsonic Mach wave domain (when the primary frequency is subsonic) and supersonic (when the primary frequency is supersonic). Unfortunately, most of the experiments validating the basic theory have been comfortably above the limits set by the existing experimental work.

2.2. *Flow control*

Experiments on controlling the development of the jet plume have been going on for almost as long as jets have been in use. Applications for flow control cover a wide range of topics, but the most heavily studied are noise reduction and mixing enhancement. Previous studies of jet flow control include both passive (geometrical modifications of the nozzle such as chevrons, lobed nozzles, etc.) (e.g. Samimy, Zaman & Reeder 1993; Zaman, Reeder & Samimy 1994; Kim & Samimy 1999; Saiyed, Mikkelsen & Bridges 2003; Callender, Gutmark & Martens 2004; Viswanathan 2005) and active (can be turned off to eliminate performance penalties when not needed) control techniques (e.g. Crow & Champagne 1971; Kibens 1980; Zaman & Hussain 1980, 1981; Gutmark & Ho 1983; Ho & Huerre 1984; Cohen & Wygnanski 1987).

Jets have several instabilities which have been well researched in low-speed and low-Reynolds-number jets (e.g. Crow & Champagne 1971; Kibens 1980; Zaman & Hussain 1980, 1981; Gutmark & Ho 1983; Ho & Huerre 1984; Michalke 1984; Cohen & Wygnanski 1987; Monkewitz *et al.* 1990; Jendoubi & Strykowski 1994; Lesshafft, Huerre & Sagaut 2010). These instabilities are: the jet initial shear layer instability, the jet column or jet preferred mode instability, instability related to significant density gradients in the jet and, in the case of an axisymmetric jet, the azimuthal component of instability. More information on these instabilities and how they are relevant to the control of jets can be found in previous works (Samimy *et al.* 2007*a*, *b*, 2010; Kearney-Fischer, Kim & Samimy 2009*b*).

In experimental work simulating practical conditions, as the Reynolds number of the jet increases for a given jet diameter and dynamic viscosity, so do the background noise, the instability frequencies and the flow momentum. To operate in this environment, active control devices (actuators) must provide excitation signals of increasingly large amplitude and frequency. As a result, the limited works in the active control of high-speed and high-Reynolds-number jets used acoustic forcing to control high subsonic jets around their preferred mode (Jubelin 1980; Lu 1983; Ahuja & Blakney 1985). There have been a few experiments which used active control in supersonic jets (e.g. Troutt & McLaughlin 1982; Morrison 1983; Ahuja and Blakney 1985; Ahuja and Whiffen 1985; Lepicovsky *et al.* 1985*a*; Lepicovsky, Ahuja & Burrin 1985*b*). The most relevant conclusion of these works is that both subsonic and supersonic jets support the existence of large turbulence structures; even in the presence of shocks. As described in more detail in the works cited (as well as the sources cited within those works), a large turbulent structure is a

https://doi.org/10.1017/jfm.2011.196 Published online by Cambridge University Press

vortex whose size is of the order of the exit dimensions of the jet. Additionally, exciting supersonic jets alters their acoustic signatures in more complex ways than in subsonic jets. Unfortunately, acoustic drivers lose control authority in these highly energetic jets at Reynolds numbers (typically control authority wanes for Reynolds numbers greater than 100,000) which are too low to explore the dynamics of high-speed and high-Reynolds-number jets used most commonly in application (i.e. jet engines). Consequently, a new type of actuator is required, which can operate in this environment. For additional information on flow control mechanisms, see the following previous works (Samimy *et al.* 2007*a*, *b*, 2010).

The Gas Dynamics and Turbulence Laboratory (GDTL) has developed a class of plasma actuators, called localized arc filament plasma actuators (LAFPAs) that can provide excitation signals of high amplitude and high frequency for high-speed and high-Reynolds-number flow control (Samimy *et al.* 2004; Kim *et al.* 2010). While plasmas have become a popular means of active flow control in recent years, LAFPAs utilize a different plasma formation process from those used in the past. For example, McLaughlin, Morrison & Troutt (1975) and Benard *et al.* (2008) used glow discharge and dielectric barrier discharge, respectively. These previous plasma types suffer from many of the same control limitations as acoustic drivers. GDTL has used these actuators for noise and flow control studies in both subsonic and supersonic unheated jets (e.g. Samimy *et al.* 2007*a*, *b*, 2010; Kim, Kastner & Samimy 2009). More recently, GDTL started exploring the impact of jet temperature on the effectiveness of LAFPAs. The effect of heating on LAFPA performance for both mixing enhancement and noise mitigation is currently under investigation in both subsonic and supersonic jets (e.g. Kearney-Fischer, Kim & Samimy 2009*a*, *b*, 2010; Kearney-Fischer & Samimy 2010). Information on the operation and performance of LAFPAs can be found in the mentioned references so it is only summarized here.

3. Experimental set-up

All the experiments are being conducted at GDTL within the Aeronautical and Astronautical Research Laboratories (AARL) at The Ohio State University. The compressed air, supplied with three five-stage reciprocating compressors, is filtered, dried and stored in two cylindrical tanks with a volume of 43 m^3 and pressure up to 16 MPa. The compressed air is passed through a storage heater at a set temperature to heat up the air to the desired temperature and supplied to the stagnation chamber of the jet facility with an axisymmetric nozzle. The air is discharged horizontally through the nozzle into an anechoic chamber and then through an exhaust system to the outdoors (figure 1*a*). The nozzles for the experiments reported in this paper are all stainless steel, axisymmetric with an exit diameter of $D = 0.0254$ m (1 in.). The nozzles are converging (operated at Mach 0.9) or converging–diverging, designed by the method of characteristics using the inviscid assumption and operated at the design points of Mach 1.3 and 1.65.

3.1. *Actuators*

Each actuator consists of a pair of pin electrodes held in place using a nozzle extension. The electrodes are distributed around the nozzle perimeter, approximately 1 mm upstream of the nozzle extension exit plane. A ring groove of 0.5 mm deep and 1 mm wide is used to house the electrodes and to shield the plasma. The nozzle extension is made of boron nitride and tungsten wires of 1 mm diameter are used for electrodes. Measured centre-to-centre, the spacing between a pair of electrodes

https://doi.org/10.1017/jfm.2011.196 Published online by Cambridge University Press

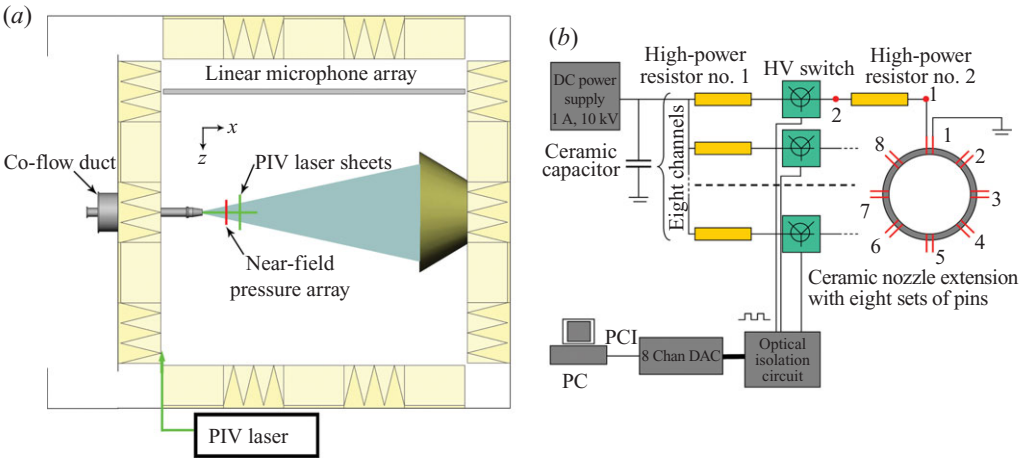


FIGURE 1. (Colour online available at journals.cambridge.org/FLM) Experimental set-up drawings. (*a*) Jet facility and anechoic chamber, (*b*) LAFPA circuit schematic.

for each actuator is 4 mm, and the distance between the neighbouring electrodes of two adjacent actuators is 6 mm. With this arrangement, eight actuators are uniformly distributed around the nozzle extension so that the azimuthal spacing between two adjacent actuators is 45°.

A multi-channel high-voltage plasma generator, designed and built in-house at The Ohio State University, is used to drive the actuators. The plasma generator enables simultaneous powering of up to eight LAFPAs distributed around the perimeter of the ceramic nozzle extension, with independent frequency, duty cycle and phase control of individual actuators. A schematic of the LAFPA circuitry is shown in figure 1(*b*). Each actuator is connected in series with a fast-response, high repetition rate, high-voltage transistor switch, two approximately 15 kΩ high-power solid-body ceramic ballast resistors and a high-voltage, high-current (10 kV, 1A) Glassman DC power supply. Two of these power supplies are used to energize eight actuators. If all eight actuators are powered at the same time, the single-actuator average current is limited to 0.25A. The switches are controlled using a multi-channel transistor–transistor logic (TTL) output peripheral component interconnect (PCI) card manufactured by the Measurement Computing Corporation and controlled by LabView software. The software generates separate pulse trains for each channel providing independent frequency, duty cycle and phase control. The switches are capable of producing high-voltage pulses (up to 10 kV) at repetition rates from 0 to 200 kHz, with a very short pulse rise/fall time (∼0.1 μs) and a variable duty cycle (from 0% to 100%). Every switch is liquid cooled to allow continuous operation at high frequencies, high voltages and high currents. Due to the physics of these actuators, their output has a square-wave nature containing only a 'positive' swing rather than the sinusoidal output of acoustic drivers. Additionally, the finite number of actuators limits the azimuthal modes available for excitation. The azimuthal modes of forcing possible for an eight-actuator configuration are $m = 0$–3, ±1, ±2 and ±4. One consequence of these arrangements is that the excitation leaks a fraction of the energy into azimuthal modes other than the one intended – this is true for any discrete actuation method (e.g. Bechert & Pfizenmaier 1977) – and also into higher frequencies. In the vast majority of cases, however, this leakage (pertaining to the phase-locked examination of large-scale structures) is not significant as evidenced by the flow-field results in

https://doi.org/10.1017/jfm.2011.196 Published online by Cambridge University Press

this and other publications on LAFPAs. For all of the azimuthal modes discussed in this paper, each actuator fires once per forcing period and each actuator imparts the same amount of energy to the flow as any other actuator. The only difference is that, in the case of $m = 0$, the peak power is eight times higher since all eight actuators fire together. In the special case of $m = \pm 1$, two of the eight actuators do not fire, but since this mode is only briefly included, it is omitted from the discussion on this page. Thus, the energy imparted to the flow per period is the same regardless of the azimuthal mode. More information on the discharge power characteristics of the actuators can be found in Utkin *et al.* (2007) and Adamovich *et al.* (2009).

3.2. *Acoustic data acquisition*

Far-field sound pressure level (SPL) is measured using 1/4 in. Bruel & Kjaer 4939 microphones. Acoustic data are collected using a linear microphone array with 10 microphones measuring angles of $\phi = 25^\circ, 30^\circ, 35^\circ, 40^\circ, 45^\circ, 50^\circ, 60^\circ, 70^\circ, 80^\circ$ and 90° relative to the jet downstream axis. The array axis is parallel to the jet axis and the microphones are mounted normal to the array axis. Testing confirmed that the only observable changes in spectra acquired with the microphones mounted as described, as opposed to radial (also referred to as normal) incidence, are due to the sensitivity of the microphones. The resulting radial distances from the nozzle exit to the microphones range from $49D$ (at 90°) to $116D$ (at 25°). The acoustic signal from each microphone is band-pass filtered from 20 Hz to 100 kHz, amplified by one of three four-channel Bruel & Kjaer Nexus 2690 conditioning amplifiers and acquired using National Instruments A/D boards and LabView software. The microphones are calibrated using a 114 dB, 1 kHz sine wave, and the frequency response of the microphones is flat up to 80 kHz with the microphone grid cover removed. Sample signals are collected at 200 kHz with 8192 data points per sample producing a spectral resolution of 24.4 Hz. An average SPL spectrum is obtained from the root-mean-square of 100 short-time spectra. More information on the microphone hardware is available in (Samimy *et al.* 2007*b*). Some spectrum and chamber qualification information can be found in Kearney-Fischer, Kim & Samimy (2011) and Kerechanin, Samimy & Kim (2001), respectively.

3.3. *Acoustic post-processing*

Several corrections are applied to the raw spectra to remove facility and atmospheric dependencies. The spectra are scaled to a uniform radius of $80\,r/D$ using r^{-2} scaling. Linear propagation scaling is valid because, as enumerated in the preceding paragraph, the microphone distances place all of the microphones in the acoustic far-field (i.e. in the linear propagation domain). Due to the alignment of the microphone array, it is necessary to correct the spectra for the directional sensitivity of the microphones. Calibration data, along with the known geometry of the microphone array relative to the jet are used to correct all microphones to normal incidence. The spectra are also corrected to standard day atmospheric absorption properties as prescribed by ANSI Standard S1.26-1995 (ANSI 1995). These corrections assume that the vast majority of the noise is emitted near the jet exit compared to the propagation distance to the microphones.

3.4. *Schlieren image acquisition*

Schlieren images of the jet are collected using a Z-type schlieren system. The system consists of the following components: two 20.3 cm (8 in.) diameter parabolic mirrors with a focal length of 1.83 m (6 ft), a Palflash 501 High-Intensity Illumination Flash unit, a single-edged razorblade and a Sony XCD-SX910 digital camera (1376×1024

https://doi.org/10.1017/jfm.2011.196 Published online by Cambridge University Press

pixels) with a Nikon 55 mm lens. The resulting resolution is 162 pixels per jet diameter with a usable viewing area of 6.5 x/D by 5 y/D. The collimated light passes through the jet normal to the jet axis, is refocused onto the razorblade edge and captured by the camera. The razorblade is mounted vertically so that the system is sensitive to horizontal (x-axis) refractions. The flash duration is approximately 500 ns – short enough to create a quasi-frozen flow-field for any of the cases discussed in this paper. The flash timing can be phase-locked to the forcing waveform allowing for increased signal-to-noise ratios by averaging. Typically, 30 or more instantaneous images are acquired for a particular set of parameters. Each image is contrast-stretched and then the set is averaged to produce a flow-field free of much of the fine-scale turbulence. As will be shown, phase locking the schlieren images allows for extraction of the essential flow characteristics.

3.5. *PIV data acquisition*

The jet flow velocity is measured by a LaVision particle image velocimetry (PIV) system using a camera with 2048 by 2048 pixel resolution. A Spectra Physics model SP-400 dual-head neodymium-doped yttrium aluminium garnet laser is used for the light source. A timing unit housed in a dual-processor computer synchronizes the camera and laser. The single camera used in these experiments measures two components of velocity on a streamwise plane. The time separation between two consecutive PIV images is of the order of 2 μs, which produces an approximately instantaneous velocity field. The time separation is slightly different at different temperatures and Mach numbers since the jet velocity changes. Sets of approximately 700 PIV image pairs were collected for each case to allow for sufficient statistical convergence. PIV processing consisted of a three-pass correlation routine with 64×64 pixel correlations for the first pass and 32×32 for an additional two passes with 50% correlation overlap in each pass. The spatial resolution of the velocity vectors depends on the field of view and the number of pixels used in the correlation. For these experiments, the spatial resolution was 0.10 x/D (2.7 mm). Background subtraction was used to remove spurious vectors that usually occur outside the mixing region of the jet.

It is not possible to seed the heated jet plume with liquid droplets. The high temperatures of the jet evaporate the droplets so it is necessary to use an alternative seeding technique. The seeding used in the heated jet experiments is aluminium oxide (Al_2O_3) particulates suspended in ethanol, a technique developed and used by Wernet & Wernet (1994). The solid particle seeding mixture is pressurized and injected into the jet far upstream of the nozzle exit and the ethanol evaporates leaving the particles well dispersed in the flow. However, in an unheated jet, the cooling caused by the expansion of the flow causes the ethanol to condense, creating a poorly seeded plume. Thus, the unheated jet is seeded in the traditional fashion using oil droplets of di-ethylhexyl sebacate (DEHS) atomized to a diameter comparable to the solid particles. This technique has been successfully used by GDTL in previous publications (Kearney-Fischer *et al.* 2009*b*, 2010).

A 38.1 cm (15 in.) duct is placed around the jet and upstream of the jet exit to generate a very low-speed coflow. The coflow is generated by routing a significant fraction of the ambient air entrained by the jet through the duct without the use of any fans or blowers. The coflow is seeded by a Concept Smoke Systems fogger to avoid spurious velocity vectors in the ambient air region. The average droplet size is about 1.0 μm for the coflow. A small amount of pressurized air is used to give the particles sufficient momentum to produce a clean image. It is assumed that the jet flow is not affected significantly by the coflow with a velocity of less than 3 m s^{-1}.

https://doi.org/10.1017/jfm.2011.196 Published online by Cambridge University Press

M_j	T_o/T_∞(TTR)	M_a	M_c	$Re_D \times 10^{-5}$	Peak radiation direction (ϕ)
0.9	1.0	0.83	0.43	6.12	25°
	1.5	1.02	0.47	3.65	25°
	2.0	1.18	0.50	2.57	25°
	2.5	1.32	0.53	1.98	25°
1.3	1.0	1.12	0.60	10.67	25°
	1.13	1.19	0.62	9.06	25°
	1.2	1.23	0.62	8.37	25°
	1.5	1.38	0.66	6.28	25°
	2.0	1.59	0.71	4.40	30°
	2.5	1.78	0.74	3.37	35°
1.65	1.0	1.33	0.73	16.48	25°
	1.5	1.63	0.81	9.58	35°
	2.0	1.88	0.87	6.66	40°
	2.5	2.10	0.92	5.08	45°

TABLE 1. Jet operating parameters and relevant characteristic quantities.

All of the PIV data discussed in this paper were collected for previous experiments. To discuss the details of all of these data sets would needlessly complicate the paper. If the reader is interested in the details of these PIV data sets, they should look to the following papers (Kearney-Fischer *et al.* 2009*b*, 2010; Kim *et al.* 2011).

3.6. *Experimental parameters*

The jets used in these experiments cover a wide range of conditions. The Mach numbers are 0.9, 1.3 and 1.65. The total temperature ratios (T_o/T_∞) range from 1.0 (unheated) to 2.5. Using the ideal gas law, Sutherland's formula for viscosity and the isentropic flow equations, the jet Reynolds numbers (Re_D) range from 2.06×10^5 (at $M_j = 0.9$ and $T_o/T_\infty = 2.5$) to 1.73×10^6 (at $M_j = 1.65$ and $T_o/T_\infty = 1.0$). A list of operating conditions and a few relevant parameters are enumerated in table 1. M_a is the jet acoustic Mach number (the jet exit velocity divided by the ambient speed of sound) and will always be referred to as the 'acoustic Mach number' in this paper. M_c is the theoretical convective Mach number derived for isentropic matched parallel shear layers (e.g. Thurow *et al.* 2008) – see (4.2) in § 4.4.2. The peak acoustic radiation direction with respect to the jet axis is populated from data shown in figure 5. Active control, as implemented using LAFPAs, is applied at forcing frequencies, in terms of Strouhal numbers, of $St_{DF} = 0.09$–3.0 and azimuthal modes of $m = 0$, 1, and 3. In one part of the analysis, $m = \pm 1$ is used to provide more data points, but the general analysis does not examine the flapping mode.

4. Results

The motivation for this study originated from the emergence of a new behaviour in the control response of a supersonic jet. As already mentioned, the impact of LAFPA forcing on the jet far-field acoustics is being explored by GDTL. In previous work on subsonic heated jets (Kearney-Fischer *et al.* 2009*a*), it was concluded that the impact of forcing on the acoustic far-field was qualitatively similar across all temperatures explored ($T_o/T_\infty = 1.0$–2.5). Quantitative differences were observable, but the broadband spectrum shape was not radically altered by forcing. A comparable

https://doi.org/10.1017/jfm.2011.196 Published online by Cambridge University Press

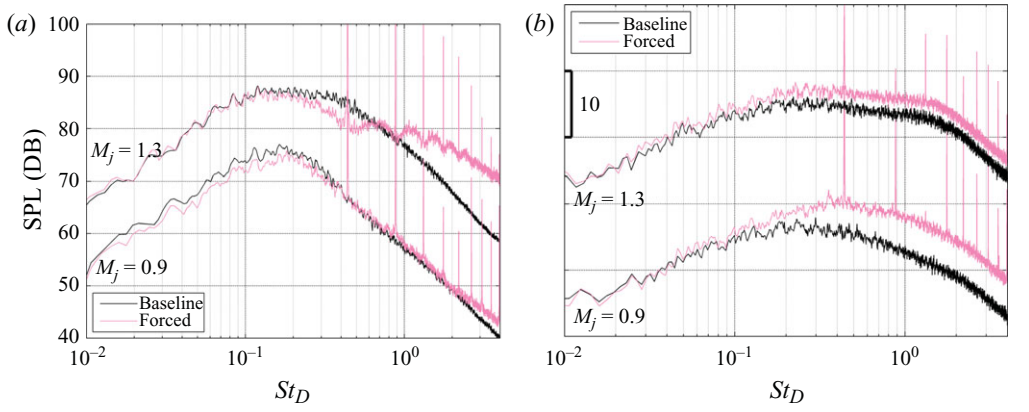


FIGURE 2. (Colour online) SPL spectra for (*a*) $\phi = 30°$ and (*b*) $\phi = 90°$ at $T_o/T_\infty = 1.5$ showing emergent behaviour in response to forcing ($m = 0$ at $St_{DF} = 0.44$) at various operating conditions.

analysis on a Mach 1.3 heated jet (Kearney-Fischer & Samimy 2010) produced some similarities, but also a major difference. Above a temperature ratio of about $T_o/T_\infty = 1.5$, the changes in metrics such as the overall SPL (OASPL) indicated that something different was happening in this low supersonic jet at a moderately elevated temperature. An examination of the narrowband spectra revealed the change. Example spectra are shown in figure 2 with pairs of forced and baseline spectra showing the far-field response of the jet to forcing. The spectra shown at the two Mach numbers ($M_j = 0.9$ and 1.3) and the same microphone locations ($\phi = 30°$ and $90°$) are for jets forced with the same forcing parameters ($m = 0$ and $St_{DF} = 0.44$). It is immediately apparent that the forcing response in the supersonic jet is very different from the subsonic case. This strong high-frequency amplification is observed to be highly directional and confined to around the peak radiation direction. Additionally, this phenomenon is dependent on the forcing parameters. Substantial alteration of the spectrum shape occurs, essentially, at frequencies around and above the forcing frequency. The high-frequency amplification observed at these conditions is not observed in the subsonic case or at the same supersonic Mach number at a lower temperature (not shown). Thus, it is concluded that this behaviour is emergent.

There are a few possible causes for this emergent behaviour, but since the response is broadband, it must be something which involves the dynamics of the jet:

(i) A change in the shock cell structure of the jet and/or a change in the nature of the flow structures which alters their dynamic interactions with the shock cells.

(ii) The emergence of Mach wave radiation as a significant component of the far-field noise, which is also related to the nature of the structures in the flow.

(iii) A previously unobserved aspect of jet dynamics.

The first possibility could occur for two likely reasons. Since the nozzle is designed using the inviscid assumption, there will always be a shock cell structure present in the jet. The gas characteristics (e.g. density, viscosity) are temperature-dependent so, as the jet temperature changes, the generated shock cell structure will also change. Secondly, the elevated temperatures produce thermal expansion in the nozzle body. The ceramic nozzle extension has a much lower thermal expansion coefficient compared to the steel nozzle body. Thus, as the materials warm up, a forward facing step could form where the nozzle and nozzle extension meet, which could alter the shock cell structure of the jet if the step is sufficiently large.

https://doi.org/10.1017/jfm.2011.196 Published online by Cambridge University Press

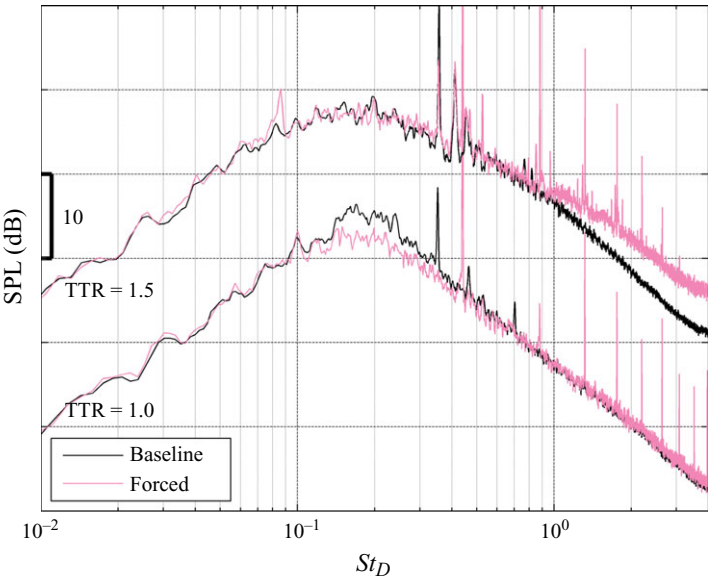


FIGURE 3. (Colour online) The 30° spectra with strong shock cell structures (generated by intentional misalignment of the nozzle and the nozzle extension) at two different temperatures in $M_j = 1.3$ forced with $m = 0$ at $St_{DF} = 0.44$.

Both of these explanations rely on the alteration of the shock cell structure as the basis for the change in forcing response. It is also reasonable to conclude that the change would be the presence of a stronger shock cell structure, since the jet is operating in the ideally expanded regime. A simple experiment was then formulated to test these possibilities. By displacing the central axis of the nozzle extension relative to the nozzle axis, a substantial step is formed which produces a comparatively strong shock cell structure. The step height of ~0.2 mm, which is roughly twice the boundary-layer momentum thickness (Kearney-Fischer *et al.* 2009*b*), is large enough that the shock structure it produces should be fairly insensitive to changes in jet temperature of the order of those under discussion here. Data are then collected over the same set of parameters to see if the altered shock cell structure produces changes in this emergent phenomenon. Data from this experiment will be referred to as the 'misaligned' configuration.

Sample SPL spectra at $\phi = 30°$ for the misaligned experiment are shown for two temperature ratios in figure 3. It is apparent from these spectra that, despite the substantial changes in the shock cell structure (as indicated by the presence of strong screech tones), the high-frequency amplification phenomenon is only observed in the elevated temperature case. Clearly, the magnitude of the amplification has been altered by the change in shock cell structure, but the phenomenon is still present and still emergent. Thus, it is concluded that a change in the shock cell structure is not responsible for this phenomenon. This experiment also eliminates any other possibilities based on geometric changes of the nozzle assembly.

Turning to the second possible cause of the high-frequency amplification, the emergence of Mach wave radiation as a significant component of jet noise has been documented, to some degree, in the literature (e.g. Papamoschou 1997; Papamoschou & Debiasi 1999; Krothapalli *et al.* 2003; Greska *et al.* 2008). However, since the transition process is continuous, determining the nature and conditions of

https://doi.org/10.1017/jfm.2011.196 Published online by Cambridge University Press

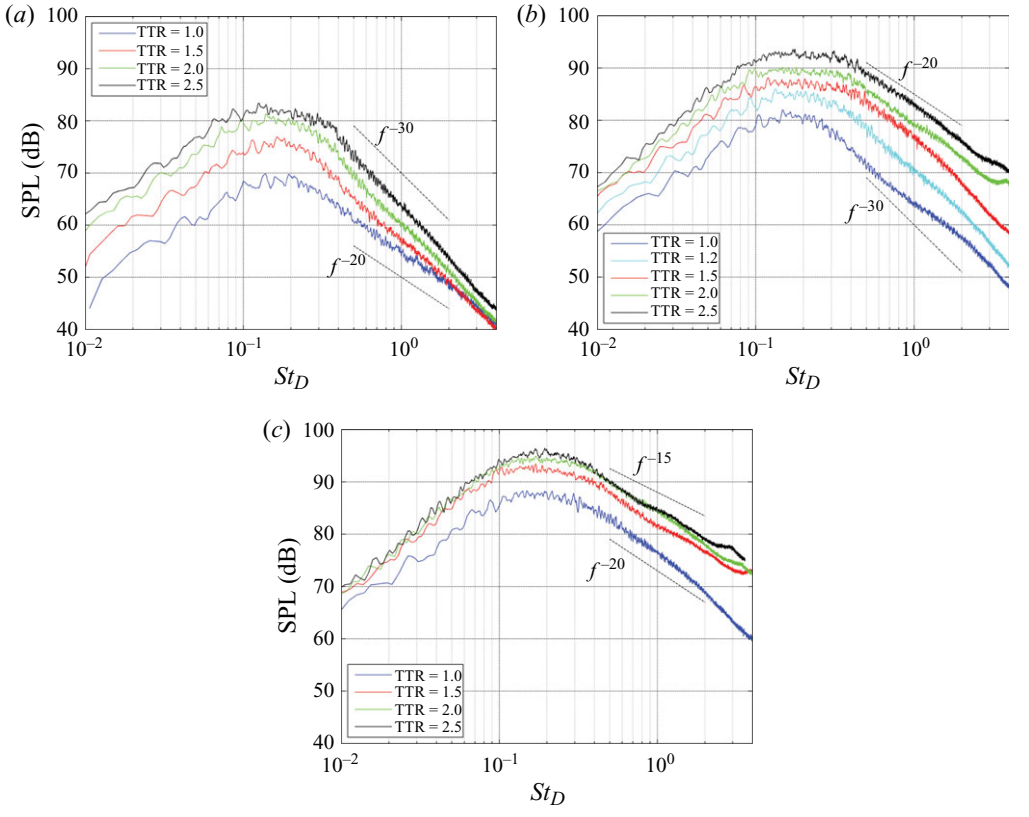


FIGURE 4. (Colour online) Baseline SPL spectra for several operating temperatures (see table 1 for measurement angles) at (*a*) $M_j = 0.9$, (*b*) $M_j = 1.3$ and (*c*) $M_j = 1.65$.

onset is considerably more difficult. The range of parameters explored in this data is documented in table 1. In this paper, the stagnation temperature ratio will be referred to as the total temperature ratio (TTR) or T_o/T_∞. While an acoustic Mach number greater than 1 indicates that some portions of the jet are moving supersonically relative to the surrounding gas, it is generally believed that the large-scale structures in the jet must be moving supersonically in order to produce Mach wave radiation. Thus, $M_a > 1$ is not a good indicator of the presence of Mach wave radiation.

The last possible explanation is included only to make the following point. Given the high improbability of discovering an entirely unknown aspect of jet dynamics which is only identifiable in a high-Reynolds-number forced jet combined with the elimination of shock cell structure or geometric changes as the cause, Mach wave radiation is the likely cause for the emergent phenomenon.

4.1. *Acoustic results – baselines*

The acoustic baselines for the three experimented jets are shown in figure 4. From this point on, the spectra discussed or used for calculation will be that of the peak radiation direction as determined from the baseline data (see figure 5 and/or table 1). Looking first at $M_j = 0.9$, as the temperature initially increases, the noise levels increase and the high-frequency roll-off steepens. Quantitative values for the high-frequency slopes are shown in table 2. These results are consistent with observations of other researchers (e.g. Viswanathan 2004; Viswanathan & Czech 2009). At the

https://doi.org/10.1017/jfm.2011.196 Published online by Cambridge University Press

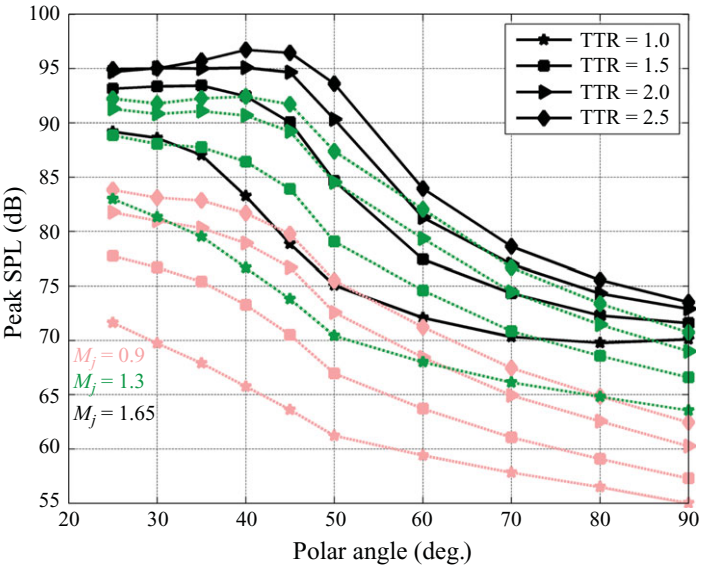


FIGURE 5. (Colour online) Peak SPL distributions for the baseline jets at the various test conditions.

highest temperatures, some peak broadening is observed and the roll-off steepening has tapered off. These changes would seem to indicate the onset of Mach wave radiation in the far-field signature, but final judgment will be reserved for later. In the $M_j = 1.3$ jet, the spectrum has the general characteristics of a mixing noise source at the lowest temperature. However, as the temperature increases, substantial peak broadening and lessening of the high-frequency roll-off rate are observed. At the highest temperature, the spectrum has a shape approaching the characteristic spectrum of a Mach-wave-radiation-dominated jet. The $M_j = 1.65$ jet is fairly broadened, even in the unheated case. As the temperature is elevated for this Mach number, the spectral characteristics stabilize indicating a completion of the transition to a Mach-wave-radiation-dominated jet. It should be noted that the increasing compressibility, indicated by high M_c, may also play a role in the evolution of the acoustic field. One additional observation about these spectra is that, while the levels and shape of the spectra change, the peak in the spectrum is always located near a Strouhal number of $St_D \approx 0.2$. This uniformity in peak radiation frequency is consistent with previous findings (e.g. Krothapalli *et al.* 2003; Viswanathan 2004).

A chart of the peak SPL at different polar angles for the various test conditions is shown in figure 5 where the symbols indicate temperature ratios and the colour indicates Mach number. The trends in the peak SPL match quite well those of the OASPL (not shown). It is clear that the SPL measured at the lowest angle is always one of the loudest. In $M_j = 0.9, \phi = 25^\circ$ is always the loudest, but in $M_j = 1.3$ and 1.65, larger angles become prominent at elevated temperatures. The change in peak radiation direction is another classic sign of Mach wave radiation dominance. It can be seen that, while the change in peak radiation direction occurs at a fairly low temperature in $M_j = 1.65\,(T_o/T_\infty \approx 1.5)$, it occurs at higher temperature in $M_j = 1.3\,(T_o/T_\infty \approx 2.0)$ and is just getting started at the highest temperature in $M_j = 0.9$. This trend is exactly what should be expected since Mach wave radiation production is related to jet velocity rather than Mach number.

https://doi.org/10.1017/jfm.2011.196 Published online by Cambridge University Press

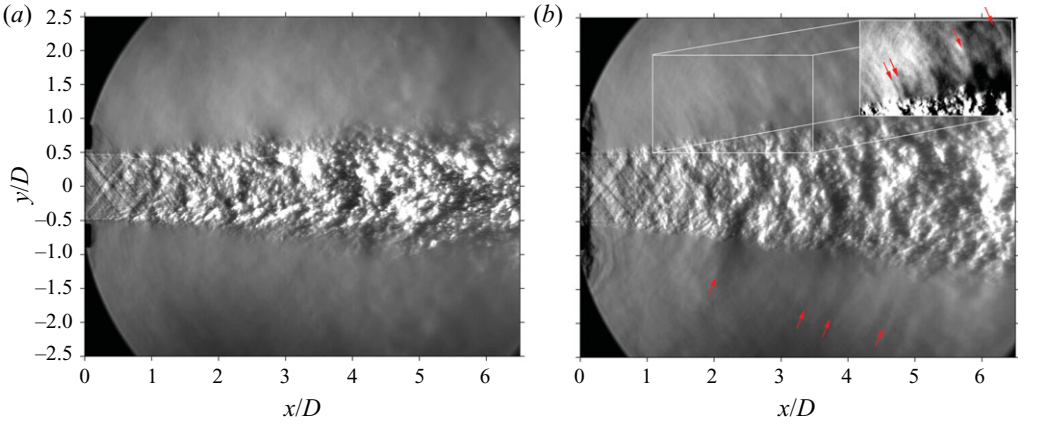


FIGURE 6. (Colour online) Instantaneous schlieren images for two baseline cases in a Mach 1.3 jet at (*a*) $T_o/T_\infty = 1.0$ and (*b*) $T_o/T_\infty = 1.5$.

The baseline spectra in figure 4 indicate that the jet is transitioning from a mixing-noise-dominated jet to a Mach-wave-radiation-dominated jet. However, due to the spatial and temporal variations of the structures present in the unforced jet, it is difficult from this data to extract when Mach wave radiation is possible, and impossible to comment on the Mach wave radiation produced by individual azimuthal modes or frequencies.

4.2. *Schlieren images*

To definitively answer the question about the existence of Mach wave radiation in these jets and its relationship to the emergent phenomenon, the schlieren system described in § 3.4 was used to visualize the density gradients in the jet. A first experiment was limited to two operating conditions: $M_j = 1.3$ at $T_o/T_\infty = 1.0$ (referred to as cold jet) and 1.5 (referred to as hot jet). These conditions were chosen because the forced spectra already discussed (figure 2) indicated that the emergent behaviour arose somewhere between these two temperature cases and the baseline acoustic data (figures 4 and 5) showed the onset of Mach wave radiation characteristics in that same range. Images were acquired at several phase angles (typically four phase angles separated by 90°) for unforced cases and $St_{DF} = 0.3$ and 0.6 at $m = 0$, 1 and 3. All of these results will be discussed, but, in the interest of space, only some will be presented.

Representative instantaneous images for the baseline at the two temperature ratios are shown in figure 6. Since the baseline flow cannot be phase-locked, an average image would not provide the needed information. The shock cell structure is initially identifiable in both images and the hot jet shows increased spreading (perhaps due to the stronger temperature/density gradients). Examining the near-field reveals the presence of some amount of Mach wave radiation in the hot jet and none in the cold jet. The radiation is fairly weak, but is still identifiable upon close inspection of the image. A few of the wavefronts are annotated with red arrows and an inset image is contrast-stretched to make the wavefronts slightly easier to identify.

Phase-averaged schlieren images are shown (figures 7*a* and 7*b*) for the cold jet forced at $St_{DF} = 0.3$ with $m = 0$ and 1. These images reveal several important aspects of the structures produced by forcing with LAFPAs. The forced structures are initially discrete (separated azimuthally as dictated by the actuator placement and firing

https://doi.org/10.1017/jfm.2011.196 Published online by Cambridge University Press

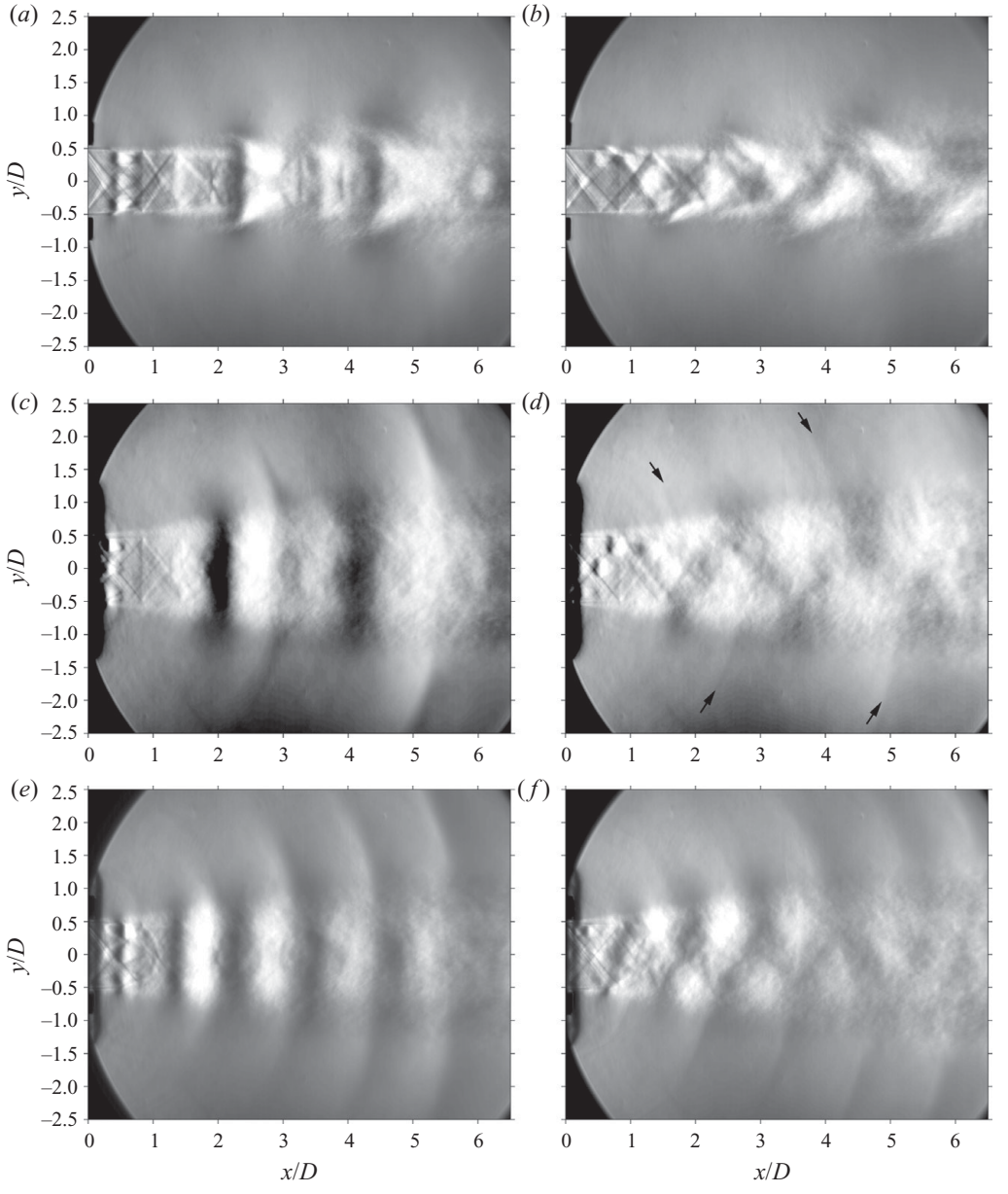


FIGURE 7. Phase-averaged schlieren images for various forced cases in a Mach 1.3 jet: (*a*) $T_o/T_\infty = 1.0, m = 0, St_{DF} = 0.3$; (*b*) $T_o/T_\infty = 1.0, m = 1, St_{DF} = 0.3$; (*c*) $T_o/T_\infty = 1.5, m = 0, St_{DF} = 0.3$; (*d*) $T_o/T_\infty = 1.5, m = 1, St_{DF} = 0.3$; (*e*) $T_o/T_\infty = 1.5, m = 0, St_{DF} = 0.6$ and (*f*) $T_o/T_\infty = 1.5, m = 1, St_{DF} = 0.6$.

pattern) and subsequently merge in various ways depending on the azimuthal mode. In $m = 0$, the discrete structures merge into a vortex ring in about one jet diameter depending on forcing frequency. The structures produced in the $m = 1$ case merge into a helix, but this requires more time than the ring merger of $m = 0$. Additionally, the impact of the structures on the hydrodynamic near-field may be observed in the form of the dark regions which extend normal to the jet axis from the vortical structures.

https://doi.org/10.1017/jfm.2011.196 Published online by Cambridge University Press

These characteristics are consistent among the various frequencies and azimuthal modes with one noteworthy exception (not shown). In $m = 3$, the initial structures never merge into a continuous structure due to azimuthal separation. Details of these structures are explored in a recent simulation paper (Gaitonde & Samimy 2010).

Phase-averaged images from the hot jet are shown for $m = 0$ and 1 at $St_{DF} = 0.3$ and 0.6 in figures 7(*c*)–7(*f*). It is clear that a strong density gradient exists adjacent to the leading edge of each structure. The Mach wave radiation produced by the forced structures is clearly stronger than in the unforced jet due to the organization induced by forcing and the absence of phase-locking in the unforced case. The observed density gradients have curvature near the structures giving a bow-shock like appearance. These images also show that the strength of the density gradients is dependent upon both azimuthal mode and forcing frequency. At $m = 1$ and $St_{DF} = 0.3$, the wavefronts are barely observable (marked with arrows) whereas they are readily observable in $m = 0$ at the same frequency. At the higher frequency, the wavefronts are readily identifiable in both $m = 0$ and $m = 1$. While not shown, it is observed that $m = 3$ produces little or no such wavefront at these conditions; likely due to the more three-dimensional nature of the coherent structures which are present in the higher azimuthal modes (Gaitonde & Samimy 2010).

The likely explanation for the existence of these density gradients is the existence of Mach wave radiation. However, Mach wave radiation shown in the literature generally consists of conical wavefronts (flat as observed in a streamwise plane). An additional experiment was performed to determine the relationship between these wavefronts and the traditionally observed Mach wave radiation. The schlieren apparatus was repositioned to capture more of the ambient field. All three jets ($M_j = 0.9$, 1.3 and 1.65) were swept through a range of temperatures ($T_o/T_\infty = 1.0$–2.5) to examine a broad range of jet velocities. The jet was forced with azimuthal mode 0 at $St_{DF} = 0.6$ – this frequency was chosen based on the schlieren images already discussed. Potential reasons for the strong response of the jet to forcing at $St_{DF} = 0.6$ are discussed in Samimy *et al.* (2010). Many combinations of temperature and jet Mach number were collected and discussed, but only a small subset of the phase-averaged images is presented in figure 8.

Looking at the trend depicted in figure 8, there is no doubt that the wavefronts already discussed are indeed Mach wave radiation. The case shown in figure 8(*a*) was chosen to see if Mach wave radiation was visible in the hottest subsonic jet produced at GDTL. While no Mach wave radiation is visible, it is possible that it is obscured by the thermal plume turbulence associated with these very hot jets since the radiation is expected to be quite weak. In figure 8(*b*), while it is quite weak, Mach wave radiation is present. What can be seen is that the hydrodynamic near-field has some curvature which was absent in the unheated jet at the same Mach number. While not presented, additional images of the $M_j = 1.3$ jet collected at temperatures between $T_o/T_\infty = 1.0$ and 1.5 show that, as the jet velocity increases, the hydrodynamic near-field develops curvature and then coalesces into the thin, but curved wavefront seen in figure 7(*e*). The remaining cases in figure 8 reveal that, as the jet velocity continues to increase and the Mach wave radiation becomes stronger, the wavefronts become flatter – characteristic of classic Mach wave radiation.

In order to better characterize the trends observed in the schlieren images, the radiation angle of the wavefronts was calculated. Using a seeded edge detection scheme, the wavefronts can be readily identified. The ends of the wavefront are determined by setting a threshold on the strength of the gradient – the change in

https://doi.org/10.1017/jfm.2011.196 Published online by Cambridge University Press

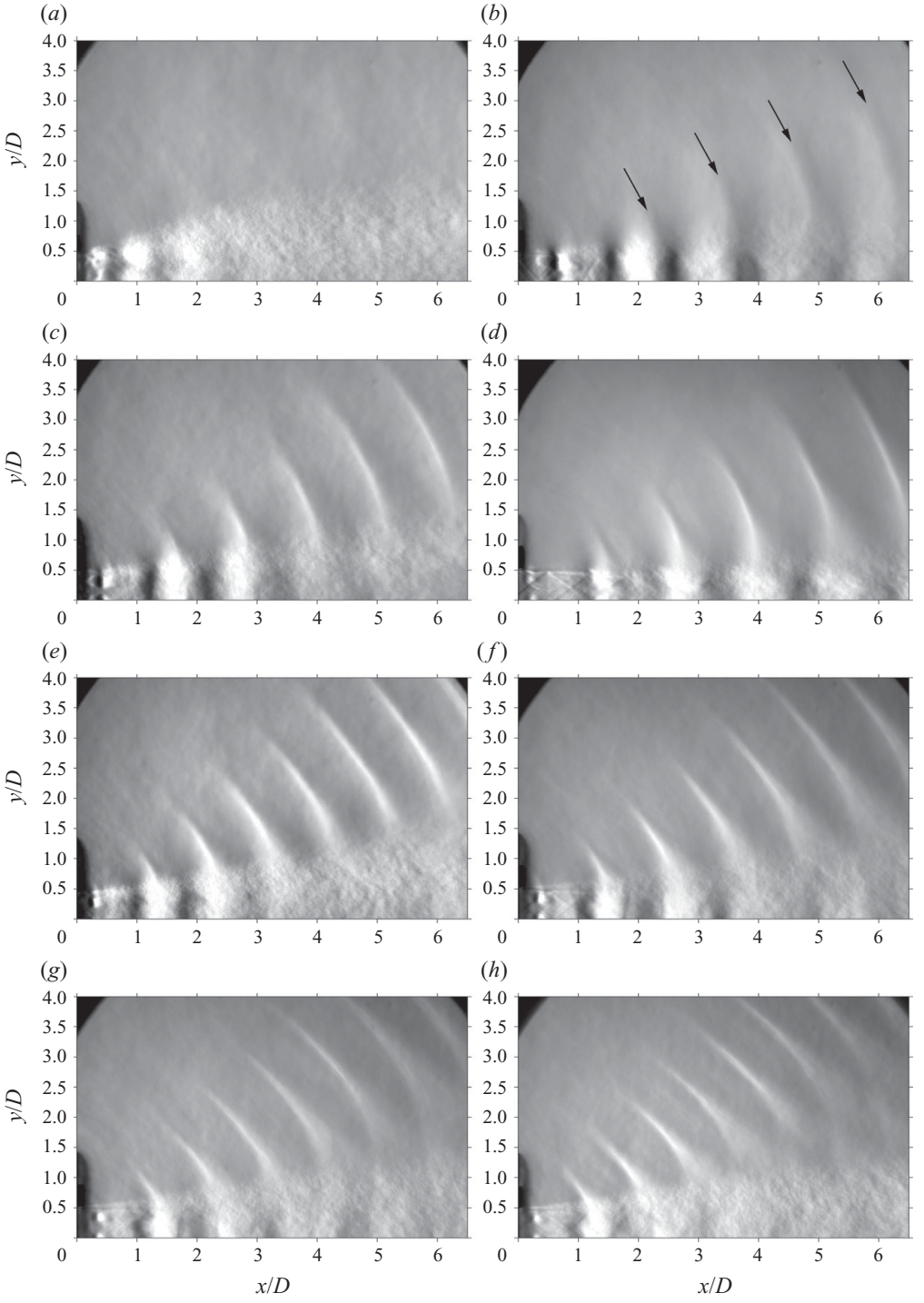


FIGURE 8. Schlieren images of jets at various operating conditions forced with $m = 0$ at $St_{DF} = 0.6$: (*a*) $M_j = 0.9$, $T_o/T_\infty = 2.5$; (*b*) $M_j = 1.3$, $T_o/T_\infty = 1.25$; (*c*) $M_j = 1.3$, $T_o/T_\infty = 1.75$; (*d*) $M_j = 1.65$, $T_o/T_\infty = 1.10$; (*e*) $M_j = 1.3$, $T_o/T_\infty = 2.5$; (*f*) $M_j = 1.65$, $T_o/T_\infty = 1.6$; (*g*) $M_j = 1.65$, $T_o/T_\infty = 2.0$ and (*h*) $M_j = 1.65$, $T_o/T_\infty = 2.5$.

https://doi.org/10.1017/jfm.2011.196 Published online by Cambridge University Press

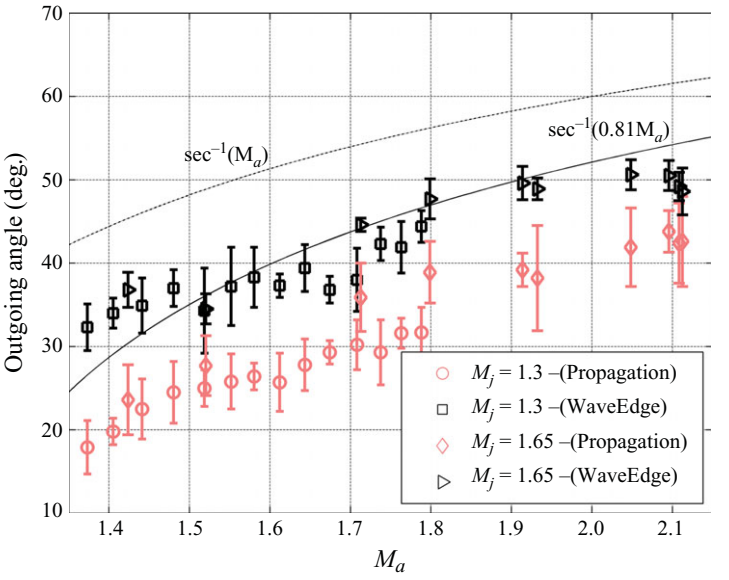


FIGURE 9. (Colour online) Mach wave radiation propagation and wave edge angles versus jet acoustic Mach number.

intensity across the wavefront normalized by the average value across the wavefront of 0.1. This threshold is somewhat arbitrary, but holding it fixed allows for a consistent identification metric. From previous works using the wavy wall analogy (e.g. Krothapalli *et al.* 2003; Tam 2009), it is known that there should exist a velocity right triangle made by the source velocity (U_x), the ambient speed of sound (a_∞), and the resulting wavefront such that $U_x/a_\infty = \sec(\theta)$. However, these studies assumed a totally flat wavefront. Thus, the wavefronts in the present study can provide the following two important pieces of information.

(i) The normal vector can be computed for every point on the wavefront. By averaging the normal vectors, the primary propagation direction of the waves (referred to as the 'propagation' angle) can be determined. The confidence interval on this quantity is determined from the standard deviation on the set of normal vectors.

(ii) Since the wavefronts are clearly not always flat, the average normal vector will under-predict the radiation angle (θ). Performing a linear fit to the outer edge of the wavefronts allows for θ (also referred to as the 'wave edge' angle) to be found. The confidence interval on θ is calculated from the uncertainty on the slope of the best fit line. Additionally, the difference between the propagation angle and the wave edge angle is a measure of the discrepancy of the observed waves from a flat wavefront.

These two quantities are plotted, along with confidence intervals, in figure 9. The data shown in this figure come from jets ranging from $M_j = 1.3$ at $T_o/T_\infty = 1.37$ (the edge detection algorithm did not work on slower jets due to the very weak wavefronts) to $M_j = 1.65$ at $T_o/T_\infty = 2.50$. As expected, the propagation angle is consistently lower than the wave edge angle. However, once jet velocity exceeds about $M_a = 2.0$, the two angles do start to converge, but are never equal. This result shows that, while the wavefronts do flatten at higher velocities, they are never completely flat. Furthermore, these results confirm something which the reader may have already observed in figure 8. In that figure, panels (c) and (d) are shown side-by-side because they have similar radiation patterns – (e) and (f) are shown side-by-side for the same

https://doi.org/10.1017/jfm.2011.196 Published online by Cambridge University Press

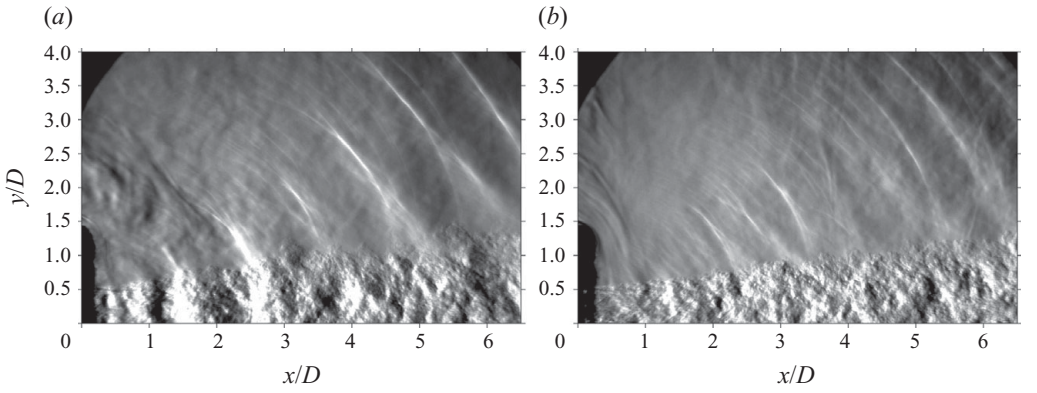


FIGURE 10. Instantaneous schlieren images for $M_j = 1.65$, $T_o/T_\infty = 1.6$ of: forced, $m = 0$, $St_{DF} = 0.6(a)$ and baseline (b).

reason. The computed radiation angles confirm what may be visually apparent. The exact relationship of these operating conditions will be discussed in greater detail in Section 4.4.2.

Two curves are also shown in figure 9. The upper curve is the predicted θ if the sources moved at the jet exit velocity. The second curve is the best fit curve of $\sec^{-1}(c\,M_a)$ to the wave edge data points assuming the source velocity is a constant fraction ($c = 0.81$) of the jet exit velocity. The data fit the curve reasonably well, but are flatter than the curve as a whole. This indicates that the source velocity is not a constant fraction of the jet exit velocity.

To prevent any misunderstanding that Mach wave radiation produced in the forced jet is clean and so should have narrowband frequency content, a representative instantaneous image is shown in figure 10(a). In this image, it may be seen that strong near-field fluctuations that survive averaging are accompanied by – and made up of – a complex pattern of structures that should produce a broadband far-field signature such as is observed in figure 2. Additionally, there exists a distribution of wavefront profiles – some are fairly flat while others are quite curved. The brightest regions of the wavefronts occur where these constituent wavefronts overlap. This can also be seen in the phase-averaged images – indicated by the fan-shaped portion of the wavefronts nearest to the jet. From the trend in the phase-averaged images, it is inferred that the curvature of a wavefront is related to the speed of the source that produced it. This instantaneous image thus shows that sources of various velocities are contributing to Mach wave radiation production at any given instant. Additionally, the repeatable superposition of the waves produced by these various sources indicates that the sources are associated with the structures produced by forcing.

An example of the Mach wave radiation from an unforced jet is shown in figure 10(b). As may be inferred from this example and many other images (not shown), all of the behaviours discussed above are also observed in the unforced jet. However, the trends are harder to identify (at least at the same operating conditions) because the wavefronts are weaker than in the forced cases and, of course, not repeatable. Therefore, it can be concluded that the jet dynamics discussed here are not unique to a forced jet. Given the transformation of the near-field forcing response, it is now reasonable to conclude that the emergent phenomenon which originally motivated this study is the onset and subsequent presence of Mach wave

https://doi.org/10.1017/jfm.2011.196 Published online by Cambridge University Press

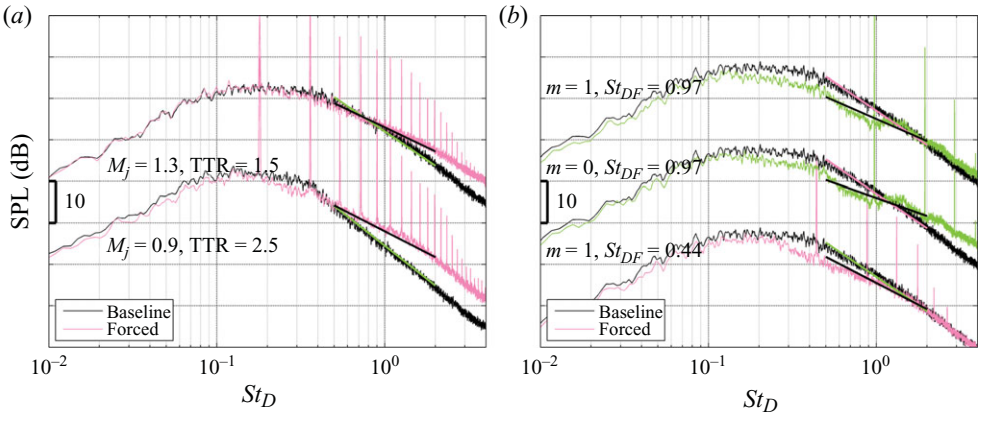


FIGURE 11. (Colour online) Example SPL spectra ($\phi = 25°$) for various cases showing parameter dependence: (*a*) $m = 0$, $St_{DF} = 0.18$ and (*b*) $M_j = 1.3$, $T_o/T_\infty = 1.5$.

radiation induced by forcing. Hereafter, the term 'emergent phenomenon' will be considered synonymous with Mach wave radiation and its use will be discontinued.

4.3. *Acoustic results – forced*

Now that the existence of forcing induced Mach wave radiation has been established, the next step is to determine the parametric domain over which this behaviour is observed and what insight this could provide into the nature of Mach wave radiation. To that end, a few more narrowband spectra will be discussed as motivation for a method of detection. Based on these spectra, a methodology is developed which can provide insight to the behaviour of the induced Mach wave radiation.

4.3.1. *Narrowband spectra*

Narrowband spectra for two different jets ($M_j = 0.9$ at $T_o/T_\infty = 2.5$ and $M_j = 1.3$ at $T_o/T_\infty = 1.5$) are shown in figure 11(*a*) with forcing parameters of $m = 0$ and $St_{DF} = 0.18$. Examining these spectra reveals that forcing induced Mach wave radiation is observable in a Mach 0.9 jet at sufficiently elevated temperatures – as one would expect. In figure 11(*b*), additional spectra for the Mach 1.3 jet with the same operating conditions as those in figure 2 are shown at different azimuthal modes and frequencies. The spectra in figures 2 and 11 illustrate that the forcing parameter and operating condition dependencies observed in the schlieren images are also detectable in the far-field acoustics.

4.3.2. *Detection methodology*

Examining the spectra presented in figures 2 and 11, the defining feature of forcing induced Mach wave radiation is a change in the slope of the high-frequency portion of the spectrum. The impact on the spectrum is of course not limited to a change in the slope, but this feature seems to be the most common and also quantifiable. The slope of the high-frequency portion of the spectrum is determined using a weighted least-squares linear fit. Using this approach, the quantity being minimized is

$$Error = \sum_i \frac{1}{f_i}(y_i - [a + b\log_{10}(f_i)])^2, \tag{4.1}$$

where a and b are the fit parameters. Weighting is necessary because the fit is performed in semi-log space. If weighting were not used, the fit would be skewed

https://doi.org/10.1017/jfm.2011.196 Published online by Cambridge University Press

	$T_o/T_\infty = 1.0$	$T_o/T_\infty = 1.5$	$T_o/T_\infty = 2.0$	$T_o/T_\infty = 2.5$
$M_j = 0.9$	−20.4	−25.7	−29.5	−32.0
$M_j = 1.3$	−23.1	−27.5	−22.3	−21.8
$M_j = 1.65$	−22.7	−19.2	−18.0	−17.2

TABLE 2. Baseline high-frequency slopes (b).

towards the high frequencies where the density of data points is highest. Thus, by weighting with the inverse of the frequency, the increase in the density of points is exactly countered by the decreased weighting. Based on inspection of the spectra, the limits of the fit were chosen as $St_D = 0.5$ (to ensure that the flat region of the peak frequencies was not included) and 2.0 (because data above this frequency were observed to be prone to jitter which obscured the trends). Sample results are shown in figure 11. This fit is performed on SPL curves (in decibels) using a Strouhal number abscissa resulting in units which are not very useful or convenient to articulate. Consequently, figures and discussion will refer to this quantity simply as 'b' with the understanding that it represents the slope in the sense of $(St_D)^b$.

4.3.3. *Spectral analysis*

Using the detection method described above, the slope 'b' is calculated for both the baseline and forced cases. The slopes for the baseline data are shown in table 2. The baseline trends were already discussed in § 4.1 and are tabulated here for completeness.

The change in the slope (Δb) relative to each baseline for the various cases is shown in figure 12. In the Mach 0.9 jet, the azimuthal modes all behave similarly (except for the $m = 0$ case at $T_o/T_\infty = 2.5$) and the changes in slope are gradual. While the changes in slope may be numerically significant, the peak values for most of the temperatures occur at frequencies well above those that substantially modulate the large-scale structures in the jet (i.e. $St_{DF} \gg 0.3$) and so are not indicative of the behaviour observed and discussed previously. However, at the highest temperature, there is some evidence of the phenomenon of interest. It is difficult to say based on figure 12(a) alone, but the supporting narrowband spectrum shown in figure 11(a) confirms that the small spike in Δb for mode 0 is indicative of the onset of Mach wave radiation.

Turning to the Mach 1.3 jet, the trends are initially similar to the Mach 0.9 jet. However, it can be seen that onset occurs somewhere between the temperature ratios of 1.13 and 1.2. As the temperature is further increased, very large changes in slope are produced. The greatest change in slope is observed at a temperature ratio of 1.5. The peak Δb then diminishes as the temperature is further increased.

In the Mach 1.65 jet, the trend begins with large peak Δb and decays to almost negligible Δb around a temperature ratio of 2.0. While not presented here, other types of acoustic analysis eliminate loss of control authority as a possible explanation for the trend observed in the Mach 1.65 data (unpublished result). It is thus observed that the Mach wave radiation induced by forcing has both an onset and a termination. The termination may be linked to compressibility effects, as will be discussed further.

Examining the trend as a whole, there are several important features, as follows.

(i) The range of the induced Mach wave radiation begins at a jet acoustic Mach number of about $M_a = 1.2$ and ends at about $M_a = 1.8$.

(ii) Onset begins at low frequencies (near or below the jet column frequency $St_{DF} = 0.3$).

https://doi.org/10.1017/jfm.2011.196 Published online by Cambridge University Press

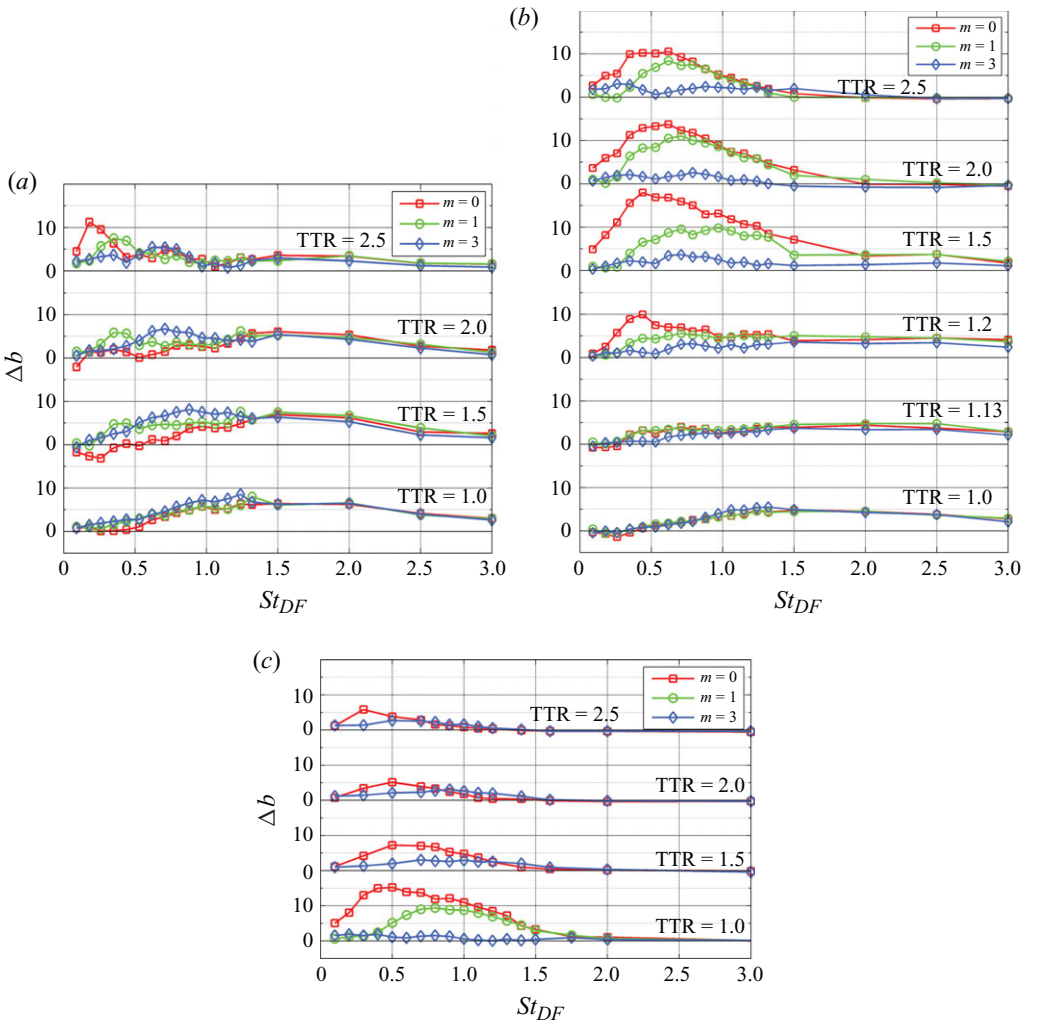


FIGURE 12. (Colour online) Change in high-frequency slope (Δb) for various cases at (*a*) $M_j = 0.9$, (*b*) $M_j = 1.3$ and (*c*) $M_j = 1.65$.

(iii) Forcing above about $St_{DF} = 1.5$ never produces a substantial effect.

(iv) Azimuthal mode 0 produces a stronger effect than any other mode.

(v) For mode 0, once the behaviour has developed, the frequency which produces the strongest effect is approximately twice the jet column natural frequency. This might be due to the development and relatively stable convection of structures created by forcing at this frequency (Samimy *et al.* 2010).

(vi) Azimuthal mode 1 does not produce a substantial effect until higher forcing frequencies. Additionally, at frequencies above about three times the jet column natural frequency, the Δb induced by mode 1 becomes similar to mode 0.

(vii) Azimuthal mode 3 never produces a detectable amount of Mach wave radiation according to this metric.

Observations 4–7 are all consistent with the conclusions drawn from the schlieren images. The additional observations provide more details on the domain of the phenomenon and further link the strength of the Mach wave radiation to the

https://doi.org/10.1017/jfm.2011.196 Published online by Cambridge University Press

nature and organization of the structures in the jet. The dependence on forcing frequency can be explained as follows. The induced Mach wave radiation production is strongest between the jet column natural instability frequency ($St_D = 0.3$) and its second harmonic ($St_D = 0.6$). The literature has shown that this frequency range produces the strongest and most coherent structures, so it is easy to see how that frequency range should produce the strongest Mach wave radiation. As the forcing frequency increases, the generated structures get smaller and have shorter lifetimes (Samimy *et al.* 2010) – consequently, the impact of forcing on Mach wave radiation production diminishes. As should be expected, research has shown that the azimuthal mode of forcing determines many aspects of the growth, interaction, and disintegration of the structures (Gaitonde & Samimy 2010). As discussed in (Gaitonde & Samimy 2010; Samimy *et al.* 2010), the structures produced by forcing with $m = 3$ (in the neighbourhood of $St_{DF} = 0.3$) are considerably smaller than those produced by axisymmetric forcing. The present results show that the axisymmetric and $m = 3$ (the highest simple azimuthal mode accessible with eight actuators) modes generate the strongest and the weakest Mach wave radiation, respectively. These coincident trends in the data support the thought process just described that larger and more coherent structures should produce more Mach wave radiation.

The last factor which likely contributes to the trends observed in the data is compressibility. Research in shear layers has shown that, as the convective Mach number (M_c) increases, the growth rate of large structures slows – resulting in a flow structure which has more three-dimensionality. As a specific example, Elliott, Samimy & Arnette (1995) observed that the structure growth rates and maximum structure sizes for a nominally two-dimensional shear layer at $M_c = 0.86$ were significantly reduced compared to a shear layer at $M_c = 0.51$. If the ability of the shear layer to amplify perturbations and roll them up into large structures is reduced, it follows that a control methodology which uses that instability mechanism would also have reduced effectiveness. Referring to table 1, $M_c = 0.86$ coincides with operating conditions at which Mach wave radiation augmentation is decreasing. However, the schlieren images (figure 8(*f*), 8(*g*) and 8(*h*)) show that forcing still maintains enough control authority to impose a stable phase reference.

4.4. *Relationship to various velocities*

In this section, the acoustic and schlieren data are interpreted in the context of various velocities to provide insight on the governing dynamics.

4.4.1. *Convective velocity*

The convective velocity of the large-scale structures is calculated from both PIV data and schlieren images. The method of calculation is slightly different for the two data sets, but both methods are centred on a one-dimensional spatial-correlation. The flow-field is cropped to typical extents of $-0.6 - 0.6\ y/D$ and $0 - 5\ x/D$. The field from each phase is then correlated with those from all other phases (including itself) in the streamwise direction. Using four phases, the correlations result in 16 independent estimates of the structure spacing (λ) that are averaged to produce a mean and confidence interval (standard deviation) for the structure spacing.

The grid resolution of the PIV data used for this analysis is about $0.1D$. The PIV data are not phase-locked to the forcing signal. In order to produce velocity fields which can be directly related to the phase-averaged schlieren images, the set of vector fields for a given case is conditionally averaged to generate a phase-averaged

https://doi.org/10.1017/jfm.2011.196 Published online by Cambridge University Press

		$T_o/T_\infty = 1.0$		$T_o/T_\infty = 1.5$	
St_{DF}	m	λ/D	U_c/a_∞	λ/D	U_c/a_∞
0.3	0	2.06 ± 0.10	0.70 ± 0.03	2.13 ± 0.15	0.88 ± 0.06
	1	1.89 ± 0.14	0.64 ± 0.05	(1.74 ± 0.32)	(0.72 ± 0.13)
0.6	0	1.07 ± 0.05	0.73 ± 0.03	1.08 ± 0.12	0.90 ± 0.10
	1	1.05 ± 0.05	0.71 ± 0.03	1.00 ± 0.13	0.83 ± 0.11

TABLE 3. Normalized structure spacing and convective velocities from $M_j = 1.3$ schlieren images.

velocity field. This technique is described in more detail in a previous publication (Kearney-Fischer *et al.* 2010). Once the conditionally averaged velocity field has been determined for the various phases, the Q-criterion (see: Jeong & Hussain 1995) is used to identify large-scale structures for each phase. The Q-criterion was chosen because it eliminates some correlated but unimportant parts of the flow-field (e.g. the regions outside the mixing layer or downstream of the end of the potential core), it converts the vector field into a scalar field, and it identifies regions of rotation and shear strain with different signs. Other than the steps mentioned here, the large-scale structure spacing calculations are the same for both the PIV and schlieren data. While it is possible to determine the large-scale structure spacing from an un-phase-locked PIV data set by spatial auto-correlation of the velocity fields, it has been verified that the results produced using the above procedure agree with the simple spatial-correlation analysis while also producing a confidence interval on the obtained result.

Using the large-scale structure spacing, the convective velocity of the structures (i.e. the propagation velocity of the large-scale structure as a single object) is then determined by means of the following analysis. In the theory of wave superposition, the group velocity is the propagation velocity of the envelope as determined by the ratio of the temporal (ω) and spatial (k) frequencies of the envelope. Since a large-scale structure is spatially and temporally localized, it contains many frequencies and wavenumbers and its velocity should thus be equated to the group velocity. Therefore, it is easy to see that the convective velocity is $U_c = \omega/k = \lambda f$, where f is the forcing frequency. The established literature (e.g. McLaughlin *et al.* 1975; Avital *et al.* 1998; Mohseni, Colonius & Freund 2002) usually examines Mach wave radiation in relation to the phase velocity of perturbations. Also, the theoretical analyses are often linear – in which case the phase velocity and group velocity are equivalent. However, only the group velocity can be extracted from the existing data. Since it is possible that non-linear behaviour (in which case, phase velocities are distinct from group velocity) plays a role in these structures, it is important to note that this discussion pertains specifically to the group velocity.

The structure spacing and convective velocities for the available schlieren and PIV data are shown in table 3 ($M_j = 1.3$ schlieren), table 4 ($M_j = 1.3$ PIV), table 5 ($M_j = 0.9$ PIV) and table 6 ($M_j = 1.65$ PIV). PIV data for the ± 1 mode are included in this section only to increase the number of available data points. On the whole, this analysis works quite well. Correlation levels were typically in the range of 0.3–0.8, but the correlation peaks did not always occur at the same locations. There are some points which have large confidence intervals (values shown in brackets). For consistency between the PIV and schlieren analyses (the PIV data have the coarser grid spacing), points with a confidence interval greater than about 2.5 times the PIV

https://doi.org/10.1017/jfm.2011.196 Published online by Cambridge University Press

		$T_o/T_\infty = 1.0$		$T_o/T_\infty = 1.5$		$T_o/T_\infty = 2.0$	
St_{DF}	m	λ/D	U_c/a_∞	λ/D	U_c/a_∞	λ/D	U_c/a_∞
0.26	0	(1.52 ± 0.56)	(0.45 ± 0.16)	(2.33 ± 0.64)	(0.84 ± 0.23)	(2.07 ± 0.30)	(0.86 ± 0.12)
	1	2.35 ± 0.09	0.69 ± 0.03	2.23 ± 0.14	0.80 ± 0.05	1.97 ± 0.20	0.82 ± 0.08
	± 1	(2.39 ± 0.32)	(0.70 ± 0.09)	2.26 ± 0.21	0.81 ± 0.08	2.24 ± 0.10	0.93 ± 0.04
0.33	0	(2.06 ± 0.32)	(0.77 ± 0.12)	1.98 ± 0.10	0.90 ± 0.05	1.82 ± 0.10	0.96 ± 0.05
	1	1.96 ± 0.07	0.73 ± 0.03	1.80 ± 0.09	0.82 ± 0.04	1.68 ± 0.09	0.88 ± 0.05
	± 1	1.91 ± 0.08	0.71 ± 0.03	1.87 ± 0.12	0.85 ± 0.05	1.82 ± 0.08	0.96 ± 0.04
0.52	0	1.31 ± 0.08	0.77 ± 0.05	1.27 ± 0.15	0.91 ± 0.11	1.25 ± 0.15	1.04 ± 0.12
	1	1.28 ± 0.02	0.75 ± 0.01	1.21 ± 0.05	0.87 ± 0.04	1.23 ± 0.08	1.02 ± 0.07
	± 1	1.30 ± 0.08	0.76 ± 0.05	1.27 ± 0.08	0.91 ± 0.06	1.26 ± 0.11	1.04 ± 0.09
1.05	0	(0.83 ± 0.36)	(0.99 ± 0.43)	(0.80 ± 0.28)	(1.16 ± 0.41)	(0.90 ± 0.40)	(1.51 ± 0.67)
	1	0.70 ± 0.03	0.83 ± 0.07	0.70 ± 0.07	1.02 ± 0.10	(None)	
	± 1	0.67 ± 0.10	0.80 ± 0.12	0.71 ± 0.05	1.03 ± 0.07	(0.79 ± 0.43)	(1.32 ± 0.72)

TABLE 4. Normalized structure spacing and convective velocities from $M_j = 1.3$ PIV data.

		$T_o/T_\infty = 1.0$		$T_o/T_\infty = 1.5$		$T_o/T_\infty = 2.0$	
St_{DF}	$\boldsymbol{m}$	λ/D	U_c/a_∞	λ/D	U_c/a_∞	λ/D	U_c/a_∞
0.33	0	1.89 ± 0.14	0.51 ± 0.04	1.66 ± 0.10	0.55 ± 0.03	1.48 ± 0.19	0.56 ± 0.07
	1	1.92 ± 0.14	0.51 ± 0.04	1.70 ± 0.13	0.56 ± 0.04	1.61 ± 0.06	0.61 ± 0.02
	± 1	1.88 ± 0.08	0.50 ± 0.02	1.72 ± 0.15	0.56 ± 0.05	1.57 ± 0.04	0.60 ± 0.02

TABLE 5. Normalized structure spacing and convective velocities from $M_j = 0.9$ PIV data.

		$T_o/T_\infty = 1.0$	
St_{DF}	m	λ/D	U_c/a_∞
0.26	0	(2.26 ± 1.02)	(0.84 ± 0.38)
	1	2.31 ± 0.14	0.86 ± 0.05
	± 1	2.51 ± 0.09	0.94 ± 0.03
0.33	0	2.12 ± 0.17	0.93 ± 0.07
	1	1.98 ± 0.07	0.87 ± 0.03
	± 1	2.14 ± 0.09	0.94 ± 0.04
0.44	0	1.69 ± 0.14	0.99 ± 0.08
	1	1.57 ± 0.08	0.92 ± 0.05
	± 1	1.63 ± 0.09	0.96 ± 0.05
0.66	0	1.15 ± 0.13	1.01 ± 0.11
	1	1.14 ± 0.15	1.00 ± 0.13
	± 1	1.12 ± 0.12	0.98 ± 0.11

TABLE 6. Normalized structure spacing and convective velocities from $M_j = 1.65$ PIV data.

grid spacing are excluded from further analysis. The values obtained from the PIV data agree closely with those from the schlieren data indicating that these numbers are accurate representations of the convective velocities and validates the process for PIV data sets for which there is no corresponding schlieren data. Additionally, while not tabulated in this paper, the convective velocities in this study agree fairly well ($U_c \approx 0.6U_j$–$0.8U_j$) with the values reported in the literature (e.g. Bridges 2006).

https://doi.org/10.1017/jfm.2011.196 Published online by Cambridge University Press

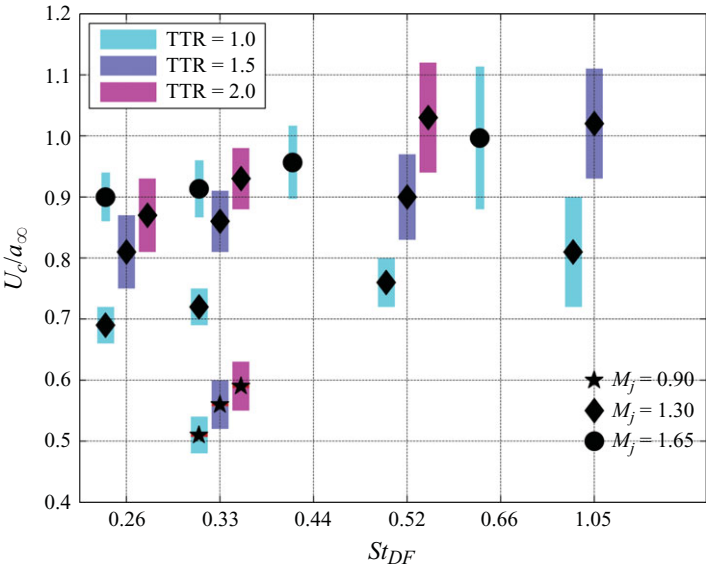


FIGURE 13. (Colour online) Azimuthal mode averaged convective velocities for various operating conditions and forcing parameters.

The most obviously important observation from this normalized convective velocity data is that many of the cases are, *on average*, moving subsonically with respect to the ambient speed of sound! The trends are a bit difficult to analyse in a table, so based on the overlap of the confidence intervals, the various azimuthal modes are averaged to create the data shown in figure 13 (the extent of the colour band denotes the confidence interval and the markers denote the Mach numbers). As one would expect, the convective velocity increases with increasing temperature for a given jet Mach number. Additionally, it can be seen that the convective velocity increases with increasing forcing frequency for a given operating condition. It can also be seen that the available convective velocities from the Mach 0.9 data do not overlap those from the Mach 1.3 data. Since the forcing parameters for which Mach wave radiation onset is observed in the acoustic data are not represented in the convective velocity data, this possibility cannot be explored. However, the Mach 1.65 data for a cold jet overlaps the Mach 1.3 data just as expected.

Returning to the primary purpose of these data, one might expect that, using the Mach 1.3 jet as the example, the convective velocities at a temperature ratio of 1.0 would be subsonic while those at 1.5 would be supersonic. The phase-averaged data clearly show that this is not the case. While convective velocity data points at higher velocities are not available in the current data set, the trend seems to indicate that the prominence of the forcing-induced Mach wave radiation decays as the convective velocity of the structures becomes supersonic. However, since this decay point can also be associated with increased compressibility as discussed above, it cannot be concluded that the supersonic condition is a defining criterion for the termination of forcing-augmented Mach wave radiation. Combining the information from all three analyses (acoustic, schlieren images, and convective velocity), the large-scale structures in the jet are capable of producing Mach wave radiation even when moving at subsonic speeds in a phase-averaged sense. Unfortunately, it is not possible

https://doi.org/10.1017/jfm.2011.196 Published online by Cambridge University Press

to extract instantaneous convective velocity measurements from the present data to determine the extent of variation in convective velocity with time.

4.4.2. *Correlation with characteristic velocities/Mach numbers*

In examining other characteristic velocities for a correlation with the behaviour observed in the data, there are several points of coincidence to consider. These points of coincidence are gleaned from both the schlieren results (figures 8(*c*)–8(*f*) and figure 9) and the acoustic data (figure 12).

(i) The characteristic velocity (U) at $M_j = 0.9$ and $T_o/T_\infty = 2.5$ should be comparable to that of $M_j = 1.3$ and $T_o/T_\infty = 1.2$.

(ii) The U at $M_j = 1.3$ and $T_o/T_\infty = 1.5$ should be comparable to that of $M_j = 1.65$ and $T_o/T_\infty = 1.0$.

(iii) The U at $M_j = 1.3$ & $T_o/T_\infty = 2.5$ should be near the value at $M_j = 1.65$ and $T_o/T_\infty = 1.6$.

There are many characteristic velocities which could be considered, but only a few will be discussed here. The most obvious one may be the theoretical isentropic convective velocity for a matched parallel shear layer (e.g. Thurow *et al.* 2008) given by

$$U_c = \frac{a_\infty U_j + a_j U_\infty}{a_\infty + a_j}, \qquad M_c = \frac{U_c - U_\infty}{a_\infty}. \tag{4.2}$$

While this quantity (enumerated in table 1) does follow the trends of the measured convective velocity in terms of variation in temperature and hydrodynamic Mach number, it consistently underestimates the convective velocity and, of course, cannot account for the variation with forcing frequency. Additionally, it does not satisfy the points of coincidence listed above.

Another group of characteristic velocities to consider are the Oertel Mach wave producing eddy velocities (Oertel 1982). These characteristic velocities were determined by measuring the angle of the strong waves produced by the flow and are related to the three families of instability waves discussed by Tam & Hu (1989). These characteristic velocities (w, w' and w'') are given by

$$\frac{w}{a_\infty} = \frac{M_j}{1 + a_\infty/a_j}, \qquad \frac{w'}{a_\infty} = \frac{1 + M_j}{1 + a_\infty/a_j}, \qquad \frac{w''}{a_\infty} = \frac{M_j - 1}{1 + a_\infty/a_j}. \tag{4.3}$$

As discussed by Tam and Hu (1989) and Tam *et al.* (1992), these characteristic velocities are related to the following instability phenomena. The w' waves are created by Kelvin–Helmholtz instability waves. The w waves are created by a viscous instability, which occurs only in jets where the perturbation propagates supersonically with respect to both the ambient and the jet core (i.e. $U_j – V_p \geqslant a_j$ and $V_p \geqslant a_\infty$ where V_p is the propagation velocity of the perturbation). Tam and Hu (1989) called this source mechanism the 'supersonic instability family'. The jets studied in this paper are all too slow to satisfy the existence conditions for the supersonic instability family. Tam and Hu also noted that, when jet reaches this supersonic condition, the Kelvin–Helmholtz instability becomes neutrally stable. Lastly, w'' waves are Mach waves which are reflected by the jet shear layers and so trapped inside the jet. This last family of waves occurs when the perturbation propagates supersonically with respect to the jet core (i.e. $U_j - V_p \geqslant a_j$). Since the last family cannot possibly be responsible for the results observed in the schlieren images, it will not be discussed further. Based on data from Panda & Seasholtz (2002), Krothapalli *et al.* (2003) concluded that the Mach waves commonly discussed in the literature should be present in jets with

https://doi.org/10.1017/jfm.2011.196 Published online by Cambridge University Press

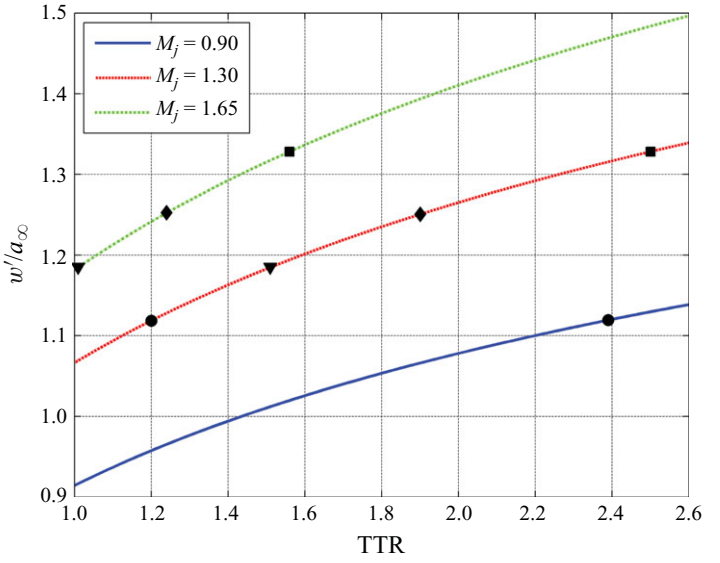


FIGURE 14. (Colour online) w'/a_∞ Oertel eddy velocity curves for various jet Mach numbers.

$w' \geqslant 1.25a_\infty$. The value of 1.25 should be treated as a rough estimate since the number of velocities in the Panda & Seasholtz paper was quite limited.

The curve for the theoretical values of w' based on isentropic calculations of the jet operating conditions is shown in figure 14. w' appears to provide a good match to the observed behaviour. This is consistent with the result of Tam *et al.* (1992), which concludes that Kelvin–Helmholtz instability waves are the dominant instability mechanism all the way up through $M_j = 2.0$ and $T_o/T_\infty = 2.5$. The required points of coincidence discussed above are marked on the figure. They highlight the points of interest for which the temperature and Mach number combination curves agree with one another. The onset coincidence (i) (marked with circles: $w' = 1.12a_\infty$) matches fairly well. The second coincidence point (ii) also matches quite well (marked with triangles: $w' = 1.185a_\infty$). The third coincidence point (iii) (marked with squares: $w' = 1.33a_\infty$), which signals the beginning of the decay of this phenomenon, likewise agrees. Additionally, when the w' eddy velocity is calculated from the radiation angle results (§4.2) as $w'/a_\infty = \sec(\theta)$, the disturbance velocities cover $w'/a_\infty = 1.09$–1.5 which aligns with the theoretical range quite well. The 1.25 estimate of Krothapalli *et al.* (marked with diamonds) lies in between the onset and decay coincidence points and provides support for the existence of Mach wave radiation in this regime. Unfortunately, w' does not match the measured phase-averaged convective velocities.

5. Discussion

As discussed in §2.1, a basic theoretical explanation for the source mechanism of Mach wave radiation has been developed and validated by simulations and experiments in the literature. One limitation of the previous works discussed in §2.1 is that this noise production mechanism is often analysed in terms of individual frequencies. Since there exist a broad range of frequencies in a turbulent jet, it is reasonable to conclude that conditions exist in which some frequencies produce Mach wave radiation while others do not. It is therefore possible that the frequency content analysed in the phase-averaged images of the current work is not inclusive of all

https://doi.org/10.1017/jfm.2011.196 Published online by Cambridge University Press

the relevant frequencies. It may be that, while the phase-averaged structures are moving subsonically, there are supersonic aspects of the structures (responsible for the observed Mach wave radiation) that do not survive averaging.

Another possible explanation for the observed behaviour is the transition to supersonic flow – referred to as the transonic regime. In this regime, there exist regions of locally supersonic flow over an object even though the velocity of the object is subsonic. If the structures in the jet are treated as solid objects (as is done in the wavy wall analogy – see § 2.1), the flow over the subsonically moving structures contains locally supersonic regions when the structure velocity is sufficiently close to sonic. The organization – including increased typical structure size – provided by forcing would cause these supersonic regions to be larger with onset at lower velocities than the smaller disordered structures of an unforced jet. However, given the highly complex shape of the structures, it is difficult to speculate on when onset of this phenomenon would occur.

The idea of structure coherence can provide some potential insight about the trends observed in forcing induced Mach wave radiation. As already discussed, compressibility is one factor that contributes to the coherence of the structures. Another factor is that, in an unforced jet, the relative phases of the various perturbation frequencies are likely to be highly erratic. The azimuthal content also plays a role in the degree of coherence. A higher order mode (e.g. $m = 3$) has lower coherence levels due to the azimuthal shape of the structures. When these factors align to produce relatively incoherent structures (e.g. a jet forced with a high frequency and high-order azimuthal mode), the resulting Mach wave radiation would be comparatively weaker and, therefore, difficult to detect. Conversely, when the jet is forced with parameters that maximize structure coherence, the Mach wave radiation is most prominent. The interaction of these factors, along with other aspects like the varying speed of different azimuthal modes (e.g. Strange & Crighton 1983; Michalke 1984; Wu 2005), results in a highly complex set of interaction dynamics. Consequently, it is difficult to say exactly which of these factors has the controlling influence on the prominence of the Mach wave radiation induced by forcing.

6. Conclusions

To better understand the behaviour of Mach wave radiation, a broad range of jet acoustic Mach numbers ($M_a = 0.83$–2.10) was explored using $M_j = 0.9$, 1.3 and 1.65 jets with stagnation temperature ratios ranging from $T_o/T_\infty = 1.0$–2.5. Both supersonic jets are generated by converging–diverging nozzles and are operated in the ideally expanded regime. The range of acoustic Mach numbers covers the previously established limits for Mach wave radiation onset of $M_a = 1.3$ (Papamoschou & Debiasi 2001). Exploration of this onset range was aided by the use of active control of the jet using plasma actuators. Data were collected using one of three systems: a linear 10-microphone far-field acoustic array with angles of $\phi = 25°$–$90°$ relative to the jet axis, schlieren and streamwise PIV. Examination of the unforced spectra shows the gradual transition from a mixing-noise-dominated jet to a Mach-wave-radiation-dominated jet as expected from previous works. Consistent with previous research, the spectrum in the peak radiation direction develops a broader and flatter spectral peak, a slower high-frequency roll off and the peak radiation direction moves to larger angles. The transition characteristics were observed to smoothly overlap between the three jet Mach numbers.

https://doi.org/10.1017/jfm.2011.196 Published online by Cambridge University Press

Forcing the jet allowed for exploration of the jet dynamics over a wide range of flow configurations (exciting combinations of one azimuthal mode $m = 0$, 1 and 3 and one Strouhal number $St_{DF} = 0.09$–3.0) by isolating a particular configuration for examination without the need for complex post-processing for azimuthal mode decomposition and frequency selection.

Phase-locked schlieren images very clearly identify the large-scale structures in the jet and also the Mach wave radiation produced by those structures. It is easily observed that the Mach waves propagate with the leading edge of the structures. Forcing organizes the flow structures which, depending on the forcing parameters, can substantially alter the nature and level of Mach wave radiation produced. Additionally, forcing reveals clear evidence of Mach wave radiation dependence on jet operating conditions, structure azimuthal mode and forcing/structure frequency. Mach wave radiation initially manifests as coalescence of the near-field hydrodynamic pressure fluctuations into curved wavefronts. As the jet velocity increases, the wavefronts flatten – eventually approaching the flat conical wavefronts characteristic of traditionally observed Mach wave radiation. Examination of both instantaneous and phase-averaged schlieren images shows that Mach wave radiation producing sources at any one operating condition move with a distribution of velocities.

Acoustic data provide more detail on the parametric dependence of Mach wave radiation production. The results show that Mach wave radiation exists (can be identified with the diagnostic methods of this paper) at jet velocities somewhat lower than previously documented ($M_a \approx 1.2$; equivalent to the Oertel Mach number $w'/a_\infty \approx 1.1$). It is also observed that the augmenting effect of forcing on Mach wave radiation production ceases as the jet operating conditions become substantially supersonic ($M_a > 1.8$ or $w'/a_\infty > 1.33$). Forcing with azimuthal mode 0 produces the greatest increases in Mach wave radiation production. Mode 1 produces equally large increases, but only at certain parameters, and $m = 3$ never produces any substantial changes in Mach wave radiation. This behaviour is likely due to the nature of the spatial coherence of the generated structures as can be seen in the schlieren images and inferred from the forcing frequency and azimuthal mode dependence, but may also be related to the different velocities of the azimuthal modes reported in the literature. From these data, it is concluded that the organization of flow structures induced by forcing has the effect of producing increased levels of Mach wave radiation in the regime where the unforced jet is transitioning from a mixing-noise-dominated to a Mach-wave-radiation-dominated jet. Forcing stops augmenting Mach wave radiation production when the baseline jet noise becomes dominated by Mach wave radiation – possibly due to the increased compressibility present in this operating regime.

Phase-averaged convective velocities for the large-scale structures were determined using one-dimensional spatial correlations between the various acquired phases of both schlieren images and PIV data. The phase-averaged convective velocities show an important result: Mach wave radiation can occur at subsonic phase-averaged convective velocities. These results also show that the dissipation of forcing-induced Mach wave radiation enhancement likely coincides with the structures attaining substantially supersonic convective velocities. However, since this point also corresponds to observations of increased compressibility in the literature, it cannot be concluded that supersonic convection with respect to ambient is the defining characteristic.

Due to the use of multiple jet Mach numbers, several points of coincidence in jet response were identified. Using these points, it was shown that the characteristic

https://doi.org/10.1017/jfm.2011.196 Published online by Cambridge University Press

velocity identified by Oertel (1982) as w' is a good indicator of the behavioural dynamics, but that it does not agree with the measured phase-averaged convective velocities. Other characteristic velocities such as the acoustic Mach number or the theoretical isentropic convective velocity for a matched parallel shear layer were shown to be poor descriptors of the observed dynamics.

In closing, the results presented in this paper show that the parameter range of Mach wave radiation production is larger than previously known. The results also indicate that the characteristics observed in the forced jet are also present in the unforced jet. Therefore, the conclusions reached about the forced jet are applicable to general jet dynamics. These experiments also show the potential of LAFPAs as a powerful diagnostic tool.

The support of this research by NASA Glenn Research Center with J. Bridges and C. Brown is greatly appreciated. The authors would also like to thank I. Adamovich and D. Gaitonde for their fruitful discussions and help.

REFERENCES

Adamovich, I., Choi, I., Jiang, N., Kim, J.-H., Keshav, S., Lempert, W. R., Mintusov, E., Nishihara, M., Samimy, M. & Uddi, M. 2009 Plasma assisted ignition and high-speed flow control: non-thermal and thermal effects. *Plasma Sources Sci. Technol.* **18**, 034018.

Ahuja, K. K. & Blakney, D. F. 1985 Tone excited jets. IV – acoustic measurements. *J. Sound Vib.* **102** (1), 93–117.

Ahuja, K. K. & Whiffen, M. C. 1985 Tone excited jets. II – flow visualization. *J. Sound Vib.* **102** (1), 63–69.

ANSI 1995 Method for calculation of the absorption of sound by the atmosphere. *American National Standards Institute* S1.26-1995.

Avital, E. J., Sandham, N. D. & Luo, K. H. 1998 Mach wave radiation by mixing layers: Part I – Analysis of the sound field. *Theor. Comput. Fluid Dyn.* **12**, 73–90.

Bechert, D. W. & Pfizenmaier, E. 1977 Amplification of jet noise by a higher-mode acoustical excitation. *AIAA J.* **15** (9), 1268–1271.

Benard, N., Bonnet, J. P., Touchard, G. & Moreau, E. 2008 Flow control by dielectric barrier discharge actuators: jet mixing enhancement. *AIAA J.* **46** (9), 2293–2305.

Bridges, J. 2006 Effect of heat on space–time correlations in jets. *AIAA Paper* 2006-2534.

Callender, B., Gutmark, E. & Martens, S. 2004 Far-field acoustic investigation into Chevron nozzle mechanisms and trends. *AIAA J.* **43** (1), 87–95.

Cohen, J. & Wygnanski, I. 1987 The evolution of instabilities in the axisymmetric jet. Part 1: the linear growth of disturbances near nozzle. *J. Fluid Mech.* **176**, 191–219.

Crow, S. C. & Champagne, F. H. 1971 Orderly structure in jet turbulences. *J. Fluid Mech.* **48** (3), 547–591.

Elliott, G. S., Samimy, M. & Arnette, S. A. 1995 The characteristics and evolution of large-scale structures in compressible mixing layers. *Phys. Fluids* **7** (4), 864–876.

Gaitonde, D. V. & Samimy, M. 2010 Effect of plasma-based azimuthal mode excitation on supersonic jet flow. *AIAA Paper* 2010-4416.

Greska, B., Krothapalli, A., Horne, W. & Burnside, N. 2008 A near-field study of high temperature supersonic jets. *AIAA Paper* 2008-3026.

Gutmark, E. & Ho, C. M. 1983 Preferred modes and the spreading rated of jets. *Phys. Fluids* **26** (10), 2932–2938.

Ho, C. M. & Huerre, P. 1984 Perturbed free shear layers. *Annu. Rev. Fluid Mech.* **16**, 365–424.

Jendoubi, S. & Strykowski, P. J. 1994 Absolute and convective instability of axisymmetric jets with external flow. *Phys. Fluids* **6** (9), 3000–3009.

Jeong, J. & Hussain, F. 1995 On the identification of a vortex. *J. Fluid Mech.* **285**, 69–94.

Jubelin, B. 1980 New experimental studies on jet noise amplification. *AIAA Paper* 1980-0961.

https://doi.org/10.1017/jfm.2011.196 Published online by Cambridge University Press

Kearney-Fischer, M., Kim, J.-H. & Samimy, M. 2009*a* Noise control of a high Reynolds number Mach 0.9 heated jet using plasma actuators. *AIAA Paper* 2009-3188.

Kearney-Fischer, M., Kim, J.-H. & Samimy, M. 2009*b* Control of a high Reynolds number Mach 0.9 heated jet using plasma actuators. *Phys. Fluids* **21**, 095101.

Kearney-Fischer, M., Kim, J.-H. & Samimy, M. 2010 Flow control of a high Reynolds number Mach 1.3 heated jet using plasma actuators. *AIAA Paper* 2010-4418.

Kearney-Fischer, M. & Samimy, M. 2010 Noise control of a high Reynolds number Mach 1.3 heated jet using plasma actuators. *AIAA Paper* 2010-13.

Kearney-Fischer, M., Kim, J.-H. & Samimy, M. 2011 Noise control of a high Reynolds number high speed heated jet using plasma actuators. *Intl J. Aeroacoust.* **10** (5-6), 491–509.

Kerechanin, C. W., II, Samimy, M. & Kim, J. H. 2001 Effects of nozzle trailing edges on acoustic field of supersonic rectangular jet. *AIAA J.* **39** (6), 1065–1070.

Kibens, V. 1980 Discrete noise spectrum generated by an acoustically excited jet. *AIAA J.* **18** (4), 434–441.

Kim, J.-H., Kastner, J. & Samimy, M. 2009 Active control of a high Reynolds number Mach 0.9 axisymmetric jet. *AIAA J.* **47** (1), 116–128.

Kim, J.-H., Kearney-Fischer, M., Samimy, M. & Gogineni, S. 2011 Far-field noise control in supersonic jets using conical and contoured nozzles. *ASME J. Engng Gas Turbines Power* **133**, 081201.

Kim, J.-H., Nishihara, M., Adamovich, I. V., Samimy, M., Gorbatov, S. V. & Pliavaka, F. V. 2010 Development of localized arc filament RF plasma actuators for high-speed and high Reynolds number flow control. *Exp. Fluids* **49** (2), 497–511.

Kim, J. & Samimy, M. 1999 Mixing enhancement via nozzle trailing edge modifications in a high speed rectangular jet. *Phys. Fluids* **11** (9), 2731–2742.

Krothapalli, A., Arakeri, V. & Greska, B. 2003 Mach wave radiation: a review and an extension. *AIAA Paper* 2003-1200.

Lepicovsky, J., Ahuja, K. K., Brown, W. H. & Burrin, R. H. 1985a Coherent large-scale structures in high Reynolds number supersonic jets. *NASA CR* 3952.

Lepicovsky, J., Ahuja, K. K., & Burrin, R. H. 1985*b* Tone excited jets. III – flow measurements. *J. Sound Vib.* **102** (1), 71–91.

Lesshafft, L., Huerre, P. & Sagaut, P. 2010 Aerodynamic sound generation by global modes in hot jets. *J. Fluid Mech.* **647**, 473–489.

Lu, H. Y. 1983 Effect of excitation on coaxial jet noise. *AIAA J.* **21** (2), 214–220.

McLaughlin, D. K., Morrison, G. L., & Troutt, T. R. 1975 Experiments on the instability waves in a supersonic jet and their acoustic radiation. *J. Fluid Mech.* **69**, 73–95.

Michalke, A. 1984 Survey on jet instability theory. *Prog. Aerosp. Sci.* **21**, 159–199.

Mohseni, K., Colonius, T. & Freund, J. B. 2002 An evaluation of linear instability waves as sources of sound in a supersonic turbulent jet. *Phys. Fluids* **14** (10), 3593–3600.

Monkewitz, P., Bechert, D., Barsikow, B. & Lehmann, B. 1990 Self-excited oscillations and mixing in a heated round jet. *J. Fluid Mech.* **213**, 611–639.

Morrison, G. L. & McLaughlin, D. K. 1979 Noise generation by instabilities in low Reynolds number supersonic jets. *J. Sound Vib.* **65** (2), 177–191.

Morrison, G. L. 1983 Effects of artificial excitation upon a low Reynolds number Mach 2.5 jet. *AIAA J.*, Technical Notes **21**(6), 920–923.

Obrist, D. 2009 Directivity of acoustic emission from wave packets to the far field. *J. Fluid Mech.* **640**, 165–186.

Oertel, H. 1982 Measured velocity fluctuations inside the mixing layer of a supersonic jet. In *Recent Contributions to Fluid Mechanics* (ed. W. Hasse), pp. 170–179. Springer-Verlag.

Panda, J. & Seasholtz, R. G. 2002 Experimental investigation of density fluctuations in high-speed jets and correlation with generated noise. *J. Fluid Mech.* **450**, 97–130.

Papamoschou, D. 1997 Mach wave elimination in supersonic jets. *AIAA J.* **35** (10), 1604–1611.

Papamoschou, D. & Debiasi, M. 1999 Noise measurements on supersonic jets treated with the Mach wave elimination method. *AIAA J.* **37** (2), 154–160.

Papamoschou, D. & Debiasi, M. 2001 Directional suppression of noise from a high-speed jet. *AIAA J.* **39** (3), 380–387.

https://doi.org/10.1017/jfm.2011.196 Published online by Cambridge University Press

Saiyed, N. H., Mikkelsen, K. L. & Bridges, J. E. 2003 Acoustics and thrust of quiet separate-flow high-bypass-ratio nozzles. *AIAA J.* **41** (3), 372–378.

Samimy, M., Adamovich, I., Webb, B., Kastner, J., Hileman, J., Keshav, S. & Palm, P. 2004 Development and characterization of plasma actuators for high-speed jet control. *Exp. Fluids* **37** (4), 577–588.

Samimy, M., Kim, J.-H., Kastner, J., Adamovich, I. & Utkin, Y. 2007*a* Active control of high-speed and high-Reynolds-number jets using plasma actuators. *J. Fluid Mech.* **578**, 305–330.

Samimy, M., Kim, J. H., Kastner, J., Adamovich, I. & Utkin, Y. 2007b Active control of a Mach 0.9 jet for noise mitigation using plasma actuators. *AIAA J.* **45** (4), 890–901.

Samimy, M., Kim, J.-H., Kearney-Fischer, M. & Sinha, A. 2010 Acoustic and flow fields of an excited high Reynolds number axisymmetric supersonic jet. *J. Fluid Mech.* **656**, 507–529.

Samimy, M., Zaman, K. B. M. Q. & Reeder, M. F. 1993 Effect of tabs on the flow and noise field of an axisymmetric jet. *AIAA J.* **31** (4), 609–619.

Seiner, J. M., Bhat, T. R. S. & Ponton, M. K. 1994 Mach wave emission from a high-temperature supersonic jet. *AIAA J.* **32** (12), 2345–2350.

Strange, P. J. R. & Crighton, D. G. 1983 Spinning modes on axisymmetric jets, Part 1. *J. Fluid Mech.* **134**, 231–245.

Tam, C. K. W. 1971 Directional acoustic radiation from a supersonic jet generated by shear layer instability. *J. Fluid Mech.* **46** (4), 757–768.

Tam, C. K. W. & Burton, D. E. 1984 Sound generated by instability waves of supersonic flows. Part 2. Axisymmetric jets. *J. Fluid Mech.* **138**, 273–295.

Tam, C. K. W. & Hu, F. Q. 1989 On the three families of instability waves of high-speed jets. *J. Fluid Mech.* **201**, 447–483.

Tam, C. K. W. 1991 Jet noise generated by large-scale coherent motion. In *Aeroacoustics of Flight Vehicles: Theory and Practice* (ed. H. H. Hubbard), *WRDC Tech. Rep.*, vol. 1, *Noise Sources*, pp. 311–390.

Tam, C. K. W., Ghen, P. & Seiner, J. M. 1992 Relationship between instability waves and noise of high-speed jets. *AIAA J.* **30** (7), 1747–1752.

Tam, C. K. W. 1995 Supersonic jet noise. *Ann. Rev. Fluid Mech.* **27**, 17–43.

Tam, C. K. W. 2009 Mach wave radiation from high-speed jets. *AIAA J.* **47**(10), 2440–2448.

Thurow, B. S., Jiang, N., Kim, J.-H., Lempert, W. & Samimy, M. 2008 Issues with measurements of the convective velocity of large-scale structures in the compressible shear layer of a free jet. *Phys. Fluids* **20**, 066101.

Troutt, T. R. & McLaughlin, D. K. 1982 Experiments on the flow and acoustic properties of a moderate-Reynolds-number supersonic jet. *J. Fluid Mech.* **116**, 123–156.

Utkin, Y. G., Keshav, S., Kim, J.-H., Kastner, J., Adamovich, I. V. & Samimy, M. 2007 Development and use of localized arc filament plasma actuators for high-speed flow control. *J. Phys. D: Appl. Phys.* **40**(3), 685–694.

Viswanathan, K. 2004 Aeroacoustics of hot jets. *J. Fluid Mech.* **516**, 39–82.

Viswanathan, K. 2005 Nozzle shaping for reduction of jet noise from single jets. *AIAA J.* **43**(5), 1008–1022.

Viswanathan, K. & Czech, M. J. 2009 Role of jet temperature in correlating jet noise. *AIAA J.* **47**(5), 1090–1106.

Wernet, J. H. & Wernet, M. P. 1994 Stabilized alumina/ethanol colloidal dispersion for seeding high temperature air flows. *NASA technical memorandum.*

Wu, X. 2005 Mach wave radiation of nonlinearly evolving supersonic instability modes in shear layers. *J. Fluid Mech.* **523**, 121–159.

Zaman, K. B. M. Q. & Hussain, A. K. M. F. 1980 Vortex pairing in a circular jet under controlled excitation. Part 1. General jet response. *J. Fluid Mech.* **101**(3), 449–491.

Zaman, K. B. M. Q. & Hussain, A. K. M. F. 1981 Turbulence suppression in free shear flows by controlled excitation. *J. Fluid Mech.* **103**, 133–159.

Zaman, K. B. M. Q., Reeder, M. F. & Samimy, M. 1994 Control of an axisymmetric jet using vortex generators. *Phys. Fluids* **6**(2), 778–793.

https://doi.org/10.1017/jfm.2011.196 Published online by Cambridge University Press